

# Effective temperatures of classical Cepheids from line-depth ratios in the *H*-band

V. Kovtyukh<sup>1,2\*</sup>, B. Lemasle<sup>3</sup>, N. Nardetto<sup>4</sup>, G. Bono<sup>5,6</sup>, R. da Silva<sup>6,7</sup>, N. Matsunaga<sup>8</sup>, A. Yushchenko<sup>9,1</sup>, K. Fukue<sup>10,11</sup>, and E. K. Grebel<sup>12</sup>

<sup>1</sup> Astronomical Observatory, Odessa National University, Shevchenko Park, UA-65014 Odessa, Ukraine

<sup>2</sup> Institut für Astronomie und Astrophysik, Kepler Center for Astro and Particle Physics, Universität Tübingen, Sand 1, 72076 Tübingen, Germany

<sup>3</sup> Agentur für Arbeit Heidelberg 69108 Heidelberg, Germany

<sup>4</sup> Université Côte d’Azur, Observatoire de la Côte d’Azur, CNRS, Laboratoire Lagrange, France

<sup>5</sup> Dipartimento di Fisica, Università di Roma Tor Vergata, via della Ricerca Scientifica 1, I-00133 Rome, Italy

<sup>6</sup> INAF – Osservatorio Astronomico di Roma, via Frascati 33, Monte Porzio Catone, I-00078 Rome, Italy

<sup>7</sup> Agenzia Spaziale Italiana, Space Science Data Center, via del Politecnico snc, I-00133 Rome, Italy

<sup>8</sup> Department of Astronomy, School of Science, The University of Tokyo, 7-3-1 Hongo, Bunkyo-ku, Tokyo 113-0033, Japan

<sup>9</sup> Astrocamp Contents Research Institute, Goyang 10329, Korea

<sup>10</sup> Laboratory of Infrared High-resolution Spectroscopy (LiH), Koyama Astronomical Observatory, Kyoto Sangyo University, Motoyama, Kamigamo, Kita-ku, Kyoto 603-8555, Japan

<sup>11</sup> Education Center for Medicine and Nursing, Shiga University of Medical Science, Seta Tsukinowa-cho, Otsu, Shiga 520-2192, Japan

<sup>12</sup> Astronomisches Rechen-Institut, Zentrum für Astronomie der Universität Heidelberg, Mönchhofstr. 12-14, 69120 Heidelberg, Germany

Accepted XXX. Received YYY; in original form ZZZ

## ABSTRACT

The technique of line depth ratios (LDR) is one of the methods to determine the effective temperature of a star. They are crucial in the spectroscopic studies of variable stars like Cepheids since no simultaneous photometry is usually available. A good number of LDR-temperature relations are already available in the optical domain, here we want to expand the number of relations available in the near-infrared in order to fully exploit the capabilities of current and upcoming near-infrared spectrographs.

We used 115 simultaneous spectroscopic observations in the optical and the near-infrared for six Cepheids and optical line depth ratios to find new pairs of lines sensitive to temperature and to calibrate LDR-temperature relations in the near-infrared spectral range. We have derived 87 temperature calibrations valid in the [4 800–6 500] K range of temperatures. The typical uncertainty for a given relation is 60–70 K, and combining many of them provides a final precision within 30–50 K. We found a discrepancy between temperatures derived from optical or near-infrared LDR for pulsations phases close to  $\phi \approx 0.0$  and we discuss the possible causes for these differences.

Line depth ratios in the near-infrared will allow us to spectroscopically investigate highly reddened Cepheids in the Galactic centre or in the far side of the disk.

**Key words:** Stars: fundamental parameters – stars: late-type – stars: supergiants – stars: variables: Cepheids

## 1 INTRODUCTION

The effective temperature  $T_{\text{eff}}$  is a fundamental parameter of stellar atmospheres. Therefore, deriving the effective temperature of a star is the most important step in the analysis of a stellar spectrum, which

enables the determination of the chemical composition of the star and of its evolutionary status.

Since by definition, the effective temperature is the temperature of a black body that produces the same total power per unit area as the observed star,  $T_{\text{eff}}$  can be derived directly by knowing the stellar luminosity and radius (e.g., Davis & Webb 1974), making interferometric techniques the best tool at our disposal. Unfortunately, interferometric measurements are currently limited to nearby stars that do not cover yet the entire parameter space. Alternatively, the infrared flux method (IRFM, Blackwell & Shallis 1977) also provides  $T_{\text{eff}}$  and the angular radius of the star by combining its integrated flux and the infrared flux in a given band. Also, the Surface Bright-

\* This research used the facilities of the Italian Center for Astronomical Archive (IA2) operated by INAF at the Astronomical Observatory of Trieste, programme OPT19A5. This research is based [in part] on data collected at the Subaru Telescope, which is operated by the National Astronomical Observatory of Japan. We are honored and grateful for the opportunity of observing the Universe from Maunakea, which has the cultural, historical, and natural significance in Hawaii.

E-mail: vkovtyukh@ukr.net

ness color relation is used to derive the angular diameter variation and the distance of Cepheids (Nardetto et al. 2023).

It becomes then possible to calibrate (spectro-)photometric techniques, for instance measuring the Paschen continuum (3647–8206 Å) to determine  $T_{\text{eff}}$  from stellar fluxes. Another (robust) method relies on  $T_{\text{eff}}$ -color calibrations (e.g., Alonso et al. 1996; Bessell et al. 1998). Photometric techniques to derive  $T_{\text{eff}}$  are however sensitive to the other atmospheric parameters of the star (for instance its metallicity [Fe/H] or its surface gravity  $\log g$ ). Moreover, it is always difficult to obtain an accurate determination of the interstellar reddening, especially for faint, distant objects in highly extincted regions, for which we have started to obtain high-resolution spectra, in particular in the near-infrared (NIR) spectral domain.

Purely spectroscopic methods might then be preferred. For instance, fitting the profile of Balmer lines (e.g., Gehren 1981) provides a good  $T_{\text{eff}}$  diagnostic (although only below  $\sim 8000$  K) thanks to their low sensitivity on  $\log g$ . Metal line diagnostics enable us to determine simultaneously the atmospheric parameters  $T_{\text{eff}}$ ,  $\log g$ , and [Fe/H] (and microturbulent velocity  $V_t$  for 1D-analyses), either by the means of their curves of growth (e.g., Cayrel & Cayrel 1963) or by ensuring that abundances of various lines from the same element show no trend with their excitation potentials (to constrain  $T_{\text{eff}}$ ) or with their equivalent width (to constrain  $V_t$ ). They can be applied even in the case of pulsating variable stars like classical Cepheids, see for instance Kovtyukh & Andrievsky (1999). Such techniques require however accurate determinations of the atomic parameters of the line (e.g., their oscillator strengths and damping constants) and they are sensitive to departures from the Local Thermodynamical Equilibrium (LTE). Continuous progress in our knowledge of the physics of stellar atmospheres and increased computing power now allows us to directly compare an observed spectrum with grids of synthetic (e.g., Recio-Blanco et al. 2006) or empirical (e.g., Ness et al. 2015) spectra.

The line depth ratios (LDR) method, which is based on the ratio of the depths of two lines having different sensitivity to  $T_{\text{eff}}$  (Gray & Johnson 1991; Gray 1994) presents the advantage of being free from reddening effects and provides a high internal precision ( $\approx 10$  K). In FGK stars, the depths of low-excitation lines of neutral atoms are highly responsive to  $T_{\text{eff}}$ , while those of high-excitation lines are relatively insensitive to  $T_{\text{eff}}$  (Gray 2005). LDR calibrations are available for dwarf and giant stars (e.g., Strassmeier & Schordan 2000; Caccin et al. 2002; Kovtyukh et al. 2003; Biazzo et al. 2004, 2006; Kovtyukh et al. 2006; Biazzo et al. 2007). Combining a large number of calibrations improves the precision of the temperature determination significantly. The concept of LDR has recently been expanded to flux ratios (FR) by Hanke et al. (2018), focussing on small wavelength domains rather than the core of absorption lines, and with exquisite absolute calibration. They have been adapted to the specifics of Cepheids by Lemasse et al. (2020).

Kovtyukh & Gorlova (2000); Kovtyukh (2007); Proxauf et al. (2018) (see also Biazzo et al. 2004, 2006) calibrated LDR for Cepheids in the optical domain. Vasilyev et al. (2017, 2018) have confirmed the validity of the line depth ratios approach using 2D numerical models of Cepheid-like variable stars, where non-local, time-dependent convection is included from first principles. Line depth ratios of Cepheids have paved the way for studying the distribution of metals in the Milky Way thin disk (Andrievsky et al. 2002a,b,c, 2004; da Silva et al. 2016, 2022; Genovali et al. 2013, 2014, 2015; Kovtyukh, Wallerstein, & Andrievsky 2005b; Kovtyukh

et al. 2022; Lemasse et al. 2007, 2008, 2013; Luck et al. 2003, 2006, 2011; Luck & Lambert 2011; Luck 2018; Martin et al. 2015; Pedicelli et al. 2010). Cepheids in the Magellanic Clouds also allow us to investigate the distribution of metals in the young population of these galaxies (Lemasse et al. 2017; Romaniello et al. 2022). Moreover, since the Large Magellanic Cloud is used to calibrate period-luminosity (PL) relations, LDR play a crucial role in investigating the possible metallicity dependence of PL relations (Romaniello et al. 2008). Finally, LDR have also been applied to old ( $>10$  Gyr) type II Cepheids (Lemasse et al. 2015; Kovtyukh et al. 2018a,b), opening a new path to investigate thick disk and halo stars.

Cepheids' LDR also allowed us to trace temperature variations over the pulsation cycle (Luck & Andrievsky 2004; Luck et al. 2008; Kovtyukh et al. 2005a; Andrievsky et al. 2005), to discover peculiar Cepheids with high lithium content, presumably crossing the instability strip for the first time (e.g., Kovtyukh, Wallerstein, & Andrievsky 2005c; Kovtyukh et al. 2019), and to investigate Cepheids pulsating in two modes simultaneously (Kovtyukh et al. 2016; Lemasse et al. 2018).

The LDR method proved to be effective when applied to optical spectra, but it is only high-resolution IR spectroscopy that makes it possible to access the most distant stars in the Galactic disk and thereby understand the structure and evolution of the Milky Way in its innermost region, where interstellar extinction presents a serious problem (Matsunaga 2017). The primary objects of surveys in this region usually have high luminosity – namely, giants and supergiants. Recently, Fukue et al. (2015) found 9 LDR- $T_{\text{eff}}$  relations using spectra of 8 stars (mainly giants) in the  $H$ -band (14 000–18 000 Å) for  $T_{\text{eff}}$  ranging from 4 000 to 5 800 K with uncertainties of  $\sim 60$  K. Later, Jian et al. (2019) increased the number of calibrations to 11 and achieved a precision of 35 K for the range  $3700 < T_{\text{eff}} < 5000$  K. Recently Afşar et al. (2023) report five new LDR- $T_{\text{eff}}$  relations found in the  $H$ -band region and 21 new relations in the  $K$ -band. Taniguchi et al. (2018) found 81 calibrations for the  $T_{\text{eff}}$  within  $3700 < T_{\text{eff}} < 5400$  K, using spectra of 9 giants in the  $Y$ - and  $J$ -band, and Jian et al. (2020) investigated the correlation between those calibrations and  $\log g$ . Subsequently, Taniguchi et al. (2021) obtained new LDR pairs of Fe I–Fe I lines for red giants and supergiants with  $T_{\text{eff}}$  of 3 500–5 500 K. For spectra in the  $Y$ - and  $J$ -band, Matsunaga et al. (2021) developed a method for simultaneously determining  $T_{\text{eff}}$  and  $\log g$  for FGK stars of all luminosity classes; in so doing, they used 13 calibrations to deduce  $T_{\text{eff}}$  and 9 calibrations to derive  $\log g$ . All those calibrations were originally obtained in the IR range for the  $Y$ -,  $J$ -,  $H$ - and  $K$ -bands; however, they were only valid for rather low temperatures, while classical Cepheids reach  $T_{\text{eff}}$  above 6 000 K.

In this paper we want to expand the number of relations available for Cepheid studies in the near-infrared range. Sect. 2 describes the near-infrared spectra we used to search for new pairs of lines well-suited as temperature indicators, as described in Sect. 3. The new LDR- $T_{\text{eff}}$  calibrations are then investigated in Sect. 4. Sect. 5 summarizes our results.

## 2 SPECTROSCOPIC MATERIAL

A large number of high-resolution spectra of six well-known bright classical Cepheids (Table 1) were obtained with GIANO (Orsilia et al. 2014), a NIR cross-dispersed echelle spectrograph, operating at the 3.6 m Telescopio Nazionale Galileo (TNG). It covers the wavelength range 9 500–24 500 Å and operates at a very high-resolving

**Table 1.** Parameters of the calibrating classical Cepheids.

Cepheid	P day	$\langle V \rangle$ mag	$\langle H \rangle$ mag	[Fe/H] dex	$M_V$ mag
$\delta$ Cep	5.3662	3.950	2.479	0.07	-3.23
X Cyg	16.3512	6.399	3.947	0.09	-4.52
S Sge	8.3823	5.618	3.845	0.08	-3.75
T Vul	4.4355	5.751	4.237	-0.05	-3.01
S Vul	68.6510	8.972	4.806	0.09	-6.19
SV Vul	44.8942	7.230	4.051	0.11	-5.70

power ( $R \approx 50\,000$ ). Optical spectra were obtained in parallel with the High Accuracy Radial velocity Planet Searcher North spectrograph (HARPS-N, Cosentino et al. 2012). HARPS-N covers a large fraction of the optical range ( $\Delta\lambda = 3900\text{--}6900\,\text{\AA}$ ) at very high resolving power ( $R \approx 100\,000$ ). The observing log is given in Table A1.

Five additional spectra (3 of them for the calibrating Cepheids) were obtained in the  $H$ -band with the Infrared Camera and Spectrograph (IRCS) at the Subaru 8.2m telescope with a resolving power of  $R \approx 20\,000$  (Kobayashi et al. 2000, see Table 2). Since we have no means to derive a priori their  $T_{\text{eff}}$  as we do not have simultaneous optical spectra for those stars, they were only used for testing the newly obtained relations.

The spectral analysis (setting the continuum position, measuring line depths and equivalent widths) was carried out using the DECH software package<sup>1</sup>. The absorption lines of Cepheids are usually fairly broad due to pressure and Doppler broadening together with a moderate rotation ( $\omega \leq 10\,\text{km/s}$ ), and their a Voigt profile can be approximated by a Gaussian. However, they may become strongly asymmetric at some phases (e.g., Nardetto et al. 2006, 2008b). For this reason, we did not fit the entire profile but measured the line depths  $R_\lambda$  (that is, between the continuum and a parabola fit of the line core) as described by Gray (1994). Typical number of data points on which we performed the parabolic fit is 4–5.

The  $H$ -band spectra, in particular, are heavily contaminated by the absorption features caused by the Earth's atmosphere when observed from ground-based facilities. We did not perform a telluric correction, which consists in removing telluric features from the spectra. Instead, we used only wavelength ranges known to be practically free of telluric lines. We cannot exclude, however, that a few spectral lines are slightly contaminated by telluric lines.

### 3 SEARCHING FOR TEMPERATURE-SENSITIVE LINE PAIRS

With the recent development of near-infrared spectrographs, it has become possible to extend the use of line depth ratios as  $T_{\text{eff}}$  indicators to this domain. Fukue et al. (2015) were the first to provide calibration relations, in the  $H$ -band ( $1.50\text{--}1.65\,\mu\text{m}$ ). However, the paucity of low-excitation lines in this wavelength range, together with the strong molecular bands and numerous telluric lines, limited the number of useful LDR pairs to nine. Such a small number limits the precision in  $T_{\text{eff}}$  to  $\approx 50\,\text{K}$  in the most favorable cases, while precisions of the order of 5–15 K can be routinely achieved in the optical thanks to a large number of available LDRs (e.g., Kovtyukh 2007; Proxauf et al. 2018). Later on, Taniguchi et al. (2018) extended this number to 81 covering the  $Y$ - and  $J$ -band.

<sup>1</sup> <http://www.gazinur.com/DECH-software.html>

### 3.1 Searching for useful lines

In this study, we adopted a new approach: first, we selected two spectra of classical Cepheids with temperatures of about 5000 and 6200 K, representative of the range of temperatures reached by this class of stars. Line depths were then measured for all the spectra, regardless of whether the lines were blended or not, also including lines that are not reliably identified. Only lines that could be measured both in the stars with  $T_{\text{eff}}$  of 5000 K and 6200 K were kept, in order to ensure that the final relations will be applicable over a broad  $T_{\text{eff}}$  range.

For these lines, we then computed the ratios of their depths,  $R_{6200}/R_{5000}$  and split them into three groups showing significant (1), moderate (2), or slight (3) variations with  $T_{\text{eff}}$ . Pairs most likely suitable for further testing were chosen from the first and third groups. We set as an additional condition that the distance between two lines composing a given pair should not exceed  $300\,\text{\AA}$ . This algorithm yielded 1500 potentially useful line pairs. Finally, the selected lines were measured in all the spectra. The 1500 potential relations were visually inspected and fitted with polynomial relations. Ultimately, only the 87 best calibrations, accurate to within 150 K, were retained. They are shown in the Appendix (Figures A1–A5).

Examining the atomic parameters of the lines in the selected calibrations allowed us to draw the two following conclusions:

- Even lines with similar excitation potentials of the lower level (EPL) can show a good correlation with temperature. This unexpected conclusion can be explained as follows: if we consider two lines with close EPLs, but different oscillator strengths ( $\log g f$ ), then at a given  $T_{\text{eff}}$  the weaker line may be located on the linear part of the curve of growth, while the stronger line lies on the horizontal part. Thus the ratio of the depths of these two lines will be sensitive to  $T_{\text{eff}}$ . An example for such a pair of lines is given in Fig. 1. As a consequence, such a calibration can only be used for a limited range of  $T_{\text{eff}}$ ; it presents however the advantage of being independent of luminosity (or  $\log g$ ). Indeed, lines with different EPLs respond differently to  $\log g$  variations.
- Although one would expect that only unblended lines should be considered (leaving only a small number of them available in the  $H$ -band, for instance), it is nevertheless possible to use strong blends to derive  $T_{\text{eff}}$  calibrations, provided that these blends change monotonically, gradually and unequivocally with the  $T_{\text{eff}}$  variations. An example for such a line pair is shown in Fig. 2, corresponding to the calibration relation 76 (see Fig. A5)
- We note in passing that in case a telluric line would accidentally superimpose on a stellar line (which is more likely to happen in the  $H$ -band), the stellar line is discarded. Spectral lines of supergiants are usually considerably wider than the telluric lines, as shown in Fig. 3. We did not use lines distorted by the influence of telluric lines.

### 3.2 Calibrating relations

For the TNG sample, the  $T_{\text{eff}}$  values used to calibrate the LDR relations have been derived from the optical HARPS-N spectra obtained quasi simultaneously. Indeed, the beginning of the exposures is shifted by only a few minutes, which is negligible since our 6 calibrating Cepheids have a period of  $\approx 5$  days and more. We used the LDR from Kovtyukh (2007) (typically 50–60 of them are available in a given HARPS-N spectrum). This ensures that the

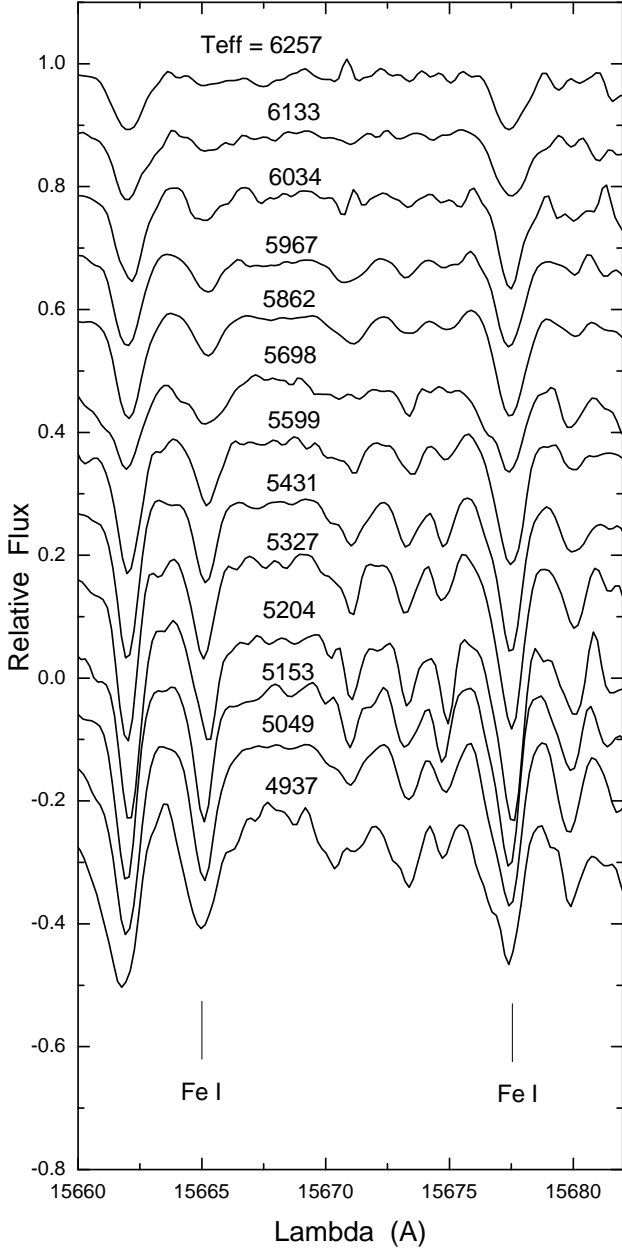


**Figure 1.** Variation of the line profile with  $T_{\text{eff}}$  for two lines with similar excitation potential of the lower level EPL, but with different oscillator strengths  $\log g f$ : the  $\text{Fe I}$  line at 15665.240 Å (EPL=5.979 eV,  $\log g f=-.336$ ) and the  $\text{Fe I}$  line at 15677.519 Å (EPL=6.246 eV,  $\log g f=0.220$ ). These two lines correspond to the calibration relation 80 (see Fig. A5).

new NIR LDR will fall on the exact same scale as those derived in the optical. We retained as calibrating  $T_{\text{eff}}$  the mean value of each temperature derived from a single calibrating relation in the optical, and the uncertainty on  $T_{\text{eff}}$  is the standard deviation of these measurements, usually around 10–30 K.

With both line depth ratios and  $T_{\text{eff}}$  values at hand, it is possible to derive analytical formulae for new calibrating relations in the near-infrared. Polynomials offer a simple way to derive analytical re-

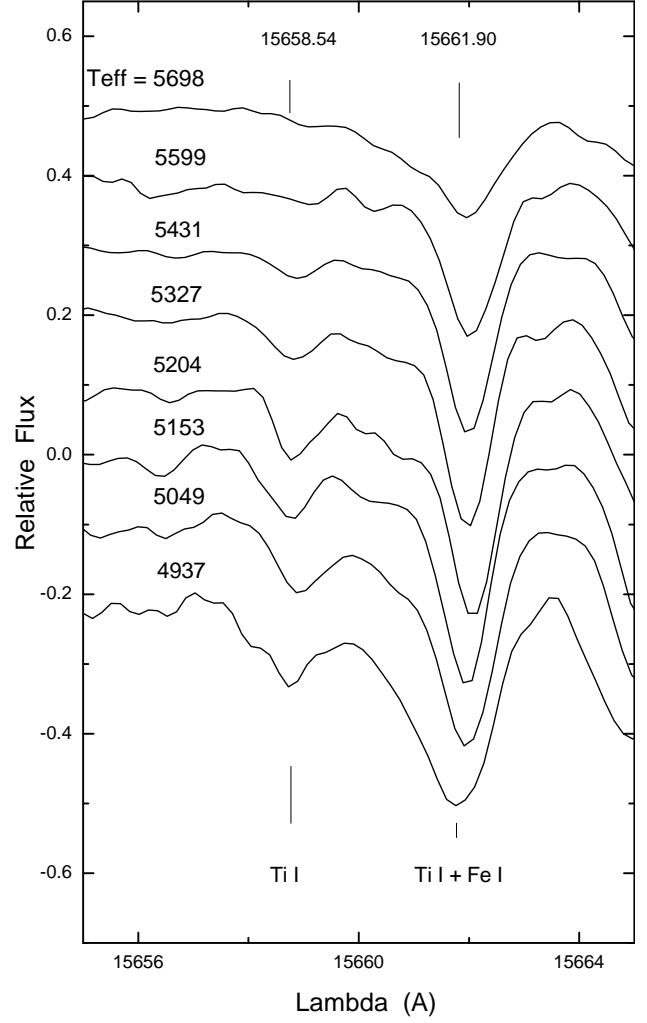


**Figure 2.** Variation of the line profile with  $T_{\text{eff}}$  for a calibration relation in which one of the lines forming the pair is blended: the first line of the ratio is the  $\text{Ti I}$  line at 15658.545 Å (EPL=5.314 eV,  $\log g f=-0.934$ ), while the second line of the ratio is a blend of two lines at 15661.898 Å ( $\text{Ti I}$ , EPL=5.172 eV,  $\log g f=-0.550$ ) and 15662.013 Å ( $\text{Fe I}$ , EPL=5.828 eV,  $\log g f=0.371$ ). Together, they form the calibration relation 76 (see Fig. A5).

lations, but a number of our calibrating relations show specific features such as breaks that cannot be adequately described even by polynomials of the 5<sup>th</sup> or higher degree (see Figs. A1–A5). Therefore, we also tried more complicated relations, such as exponential fits, logarithmic fits, power fits, the Hoerl function ( $y = ab^x x^c$ ) and others. The type of function (and the corresponding coefficients) that yielded the lowest root-mean-square deviation  $\sigma$  for a given calibration was ultimately selected.

In many cases, the precision of an individual calibration relation varies with  $T_{\text{eff}}$ . This is related to the fact that the line strengths vary with temperature. For instance, at high  $T_{\text{eff}}$ , absorption lines with low EPL become weaker, leading to greater uncertainties in the measurement of their depths, until they eventually disappear from the spectrum. To take this effect into account, we have defined as an optimum range for a given ratio the  $T_{\text{eff}}$  range within which the mean precision ( $\sigma$ ) of the calibration relation remains within 160 K.

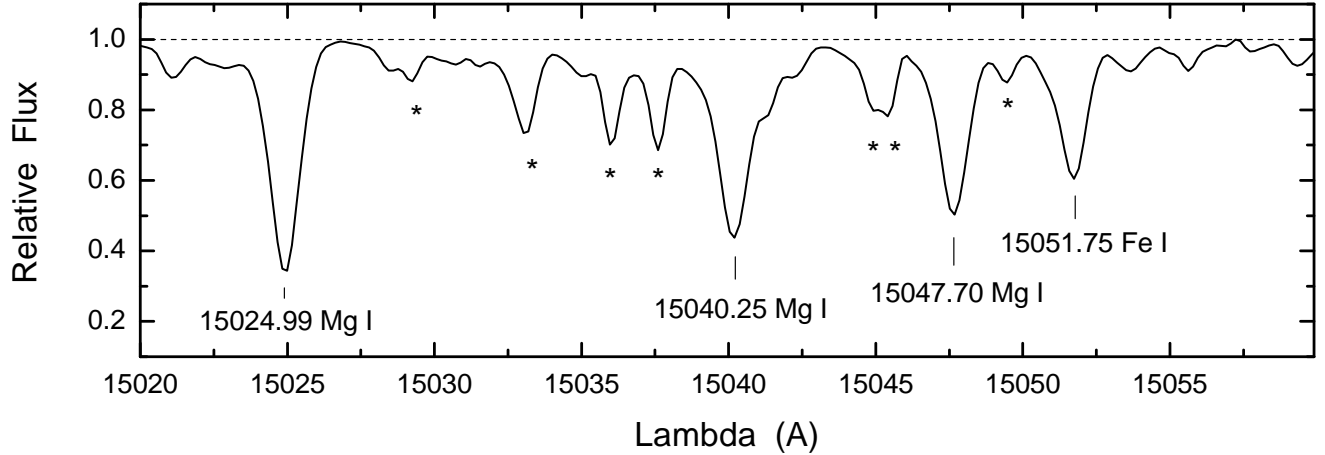


**Figure 3.** Fragment of a Cepheids' spectrum. The stellar lines are identified by their wavelengths and species, and the telluric lines are marked by asterisks.

Since various relations have various optimum ranges, we note that only a (large) subset of the 87 relations can be used for a Cepheid at a given temperature. This also holds for optical spectra and explains why the number of optical relations used to determine  $T_{\text{eff}}$  from the HARPS-N spectra varies from star to star.

Uncertainties on the line-depth measurements mainly arise from uncertainties in setting the continuum position, hence the presence of noise or telluric lines. It can be determined from lines that fall twice on adjacent orders of the echelle spectra. This uncertainty is about 2-6% for spectra with a signal-to-noise ratio of about 100. A complete analysis of the errors associated with measuring line depths in spectra is given in Catalano et al. (2002).

Besides, individual stellar parameters such as metallicity, rotation, convection, NLTE effects, magnetic fields, binarity, etc., add to the scatter of the individual calibrations. An analysis of such effects was presented in the studies by Gray (e.g., 1989, 1994); Strassmeier & Schordan (e.g., 2000); Fukue et al. (e.g., 2015).

The list of the calibrating relations, including the values for the coefficients, the intrinsic dispersion, and the applicability range, is given in Table A2 (Appendix). They are displayed in Figs. A1-A5.

#### 4 TESTING THE NEW LINE DEPTH RATIOS IN THE NIR

The temperatures inferred from both the optical and NIR spectra and their respective uncertainties are given in Table A1. A direct comparison of these temperatures is shown in Fig. 4. As can be seen, the agreement is excellent, and the largest deviations are localized for the highest  $T_{\text{eff}}$  above 6200 K.

Fig. 5 provides an alternative look to the same data, displaying the variations of  $T_{\text{eff}}$  with the pulsation phase, where  $T_{\text{eff}}$  was computed with either the HARPS-N calibration data in the optical or the new NIR relations. The latter are provided for both the GIANO spectra and the SUBARU spectra, when available (see also Table 2). Also with such a point of view, the agreement remains excellent, with the largest deviations being confined to phases close to  $\phi=0$  where  $T_{\text{eff}}$  is maximal.

We first notice that for T Vul, a classical Cepheid with the shortest period in the calibrating sample (and hence, the lowest luminosity

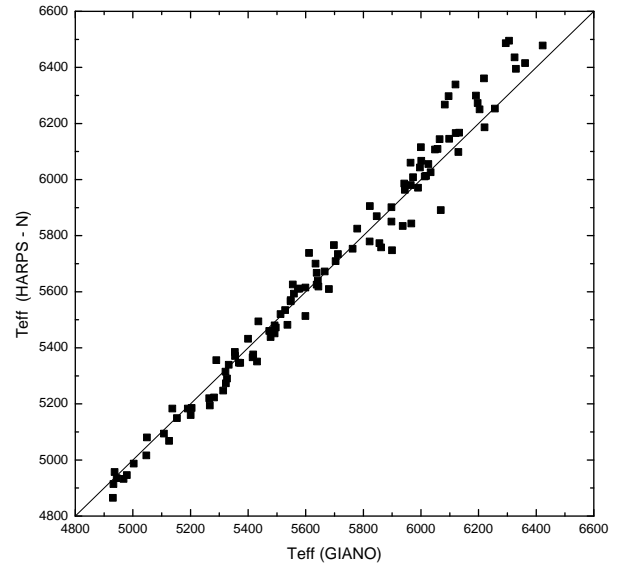


**Figure 4.** Comparison between the calibrating (optical, HARPS-N) and the retrieved (NIR, GIANO) temperatures. The 1:1 line is shown as a reference.

**Table 2.** Temperatures and associated uncertainties determined with the new LDR in the NIR for SUBARU spectra of Cepheids. The number of LDR used as well as the observing log is also provided.

Cep	P (d)	JD 2 400 000+	phase	$T_{\text{eff}}$ (K)	$\sigma$ (K)	N	$\sigma/\sqrt{N}$ (K)
CF Cas	4.8750	56137.110	.859	6047	98	18	23.1
DL Cas	8.0003	56137.080	.461	5527	116	46	17.2
$\delta$ Cep	5.3662	56136.114	.260	5843	127	17	30.7
X Cyg	16.3512	56136.105	.975	6023	162	22	34.6
SV Vul	44.8942	56137.058	.231	5760	142	21	31.0

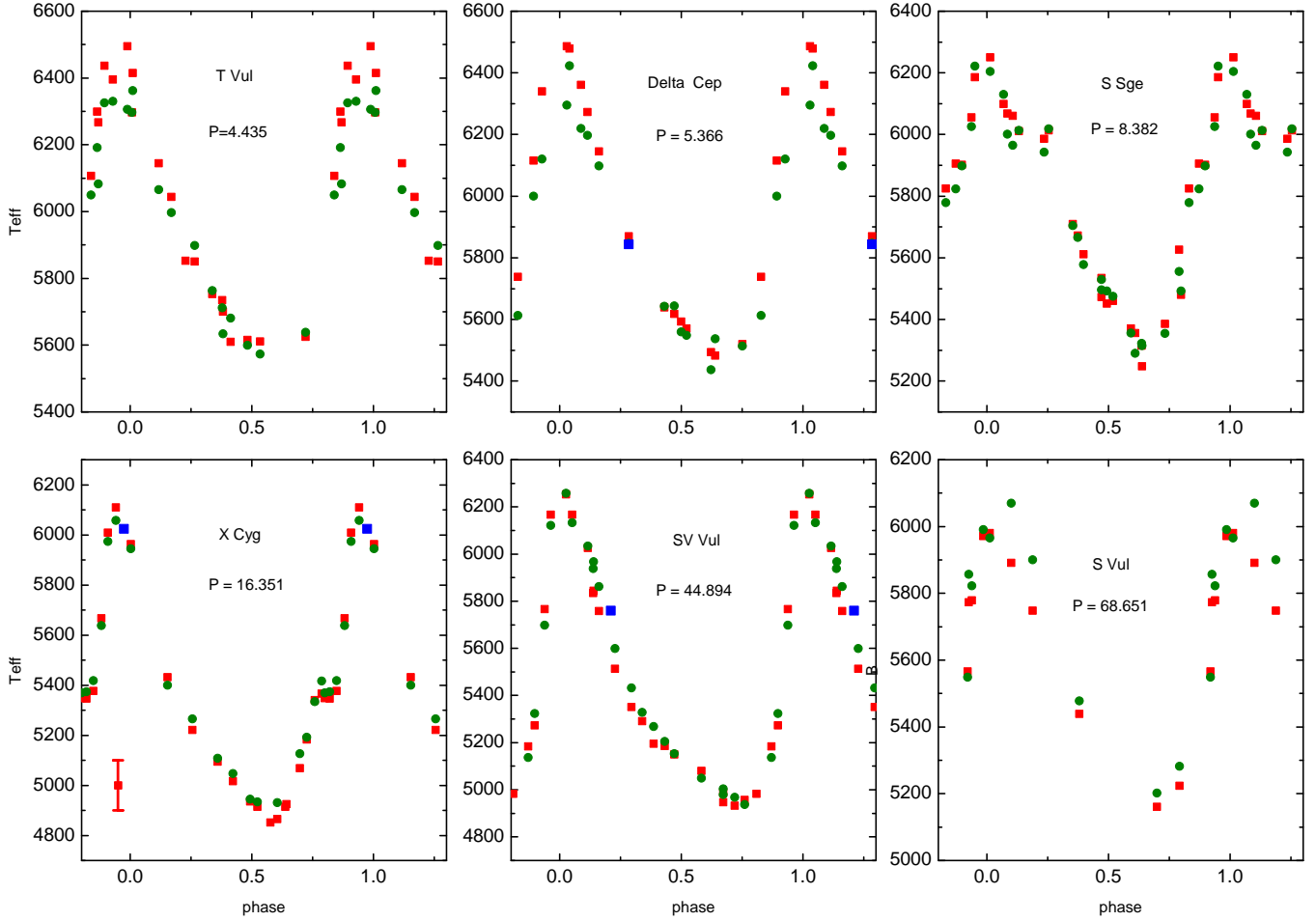


**Figure 5.** Temperature variations for the six Cepheids in the calibrating sample. Red squares: HARPS-N (optical) temperatures. A Fourier smoothing through the data points is indicated as a thin red line to guide the eye. Green circles: GIANO (near-infrared) temperatures. Blue squares: SUBARU (near-infrared) temperatures. A typical uncertainty ( $\sigma$ ) is shown in the lower-left corner of the figure. The standard errors  $\sigma / \sqrt{N}$  on individual  $T_{\text{eff}}$  measurements are smaller than the symbol sizes.

and the largest surface gravity), the NIR temperatures near the  $T_{\text{eff}}$  peak are systematically lower than those deduced from optical spectra. Conversely, for S Vul, the long-period classical Cepheid with the highest luminosity (lowest surface gravity) in the calibrating sample, the NIR temperatures are higher than those deduced from optical LDR. This points toward a luminosity (or  $\log g$ ) effect on the line depths ratios. Several (related) explanations can be proposed for such behavior.

Jian et al. (2020) already detected the effect of surface gravity on LDR. Indeed, for several pairs of lines, they noticed that the LDR– $T_{\text{eff}}$  relations were offset between dwarfs on one hand, and giants and supergiants on the other hand. They found that the difference between the ionization potentials of lines in a given pair correlates with the sensitivity of this pair to  $\log g$ . A detailed theoretical analysis of this effect can be found in Gray (2005) and Jian et al. (2020). In order to circumvent this drawback, they suggested calibrating separately dwarfs and giants/supergiants.

However, in contrast with Jian et al. (2020), who report no  $\log g$  effect within the giants-supergiants group, we find here significant  $\log g$  effects (for a narrow range of pulsation phases) for Cepheids, that is, for stars within the giants/supergiants luminosity class. We

note however that the range of luminosities for the six Cepheids in our calibrating sample is very wide and amounts to three magnitudes (their absolute magnitudes vary from  $-3$  to  $-6 M_V$ , see Table 1). This may indicate that the effect in Cepheids is not, or not only, a  $\log g$  effect. For instance,  $T_{\text{eff}}$  values may also differ due to the differences in the optical depths of the line-forming regions for the optical and IR ranges. These differences can be significant at given pulsation phases, for instance, due to the shock wave passing through the upper atmospheric layers of Cepheids near the maximum compression.

Indeed, Nardetto et al. (2018) investigated CRIRES observations of the long-period Cepheid  $\ell$  Car and found, using an hydrodynamical model of this star (Nardetto et al. 2007), that the core of the Na I line at 22 089.69 Å is formed at the top of the atmosphere, while the iron lines in the visible are formed much deeper in the atmosphere. They report additional evidence that lines in the infrared are formed closer to the surface of the star than lines in the optical, for instance the infrared radial velocity curve is shifted with respect to its optical counterpart, which they interpret as a manifestation of the Van Hoof effect (van Hoof & Struve 1953), the delay in the velocities between lines forming in the lower and upper atmosphere. Similarly, the mean radial velocity derived from infrared data differs

by  $0.53 \pm 0.30$  km s $^{-1}$  from the optical one, which they interpret as a different impact of granulation on line forming regions in the upper and lower atmosphere (the deeper the line-forming region, the more the radial velocity is blueshifted, see Nardetto et al. 2008a; Vasilyev et al. 2017).

To wrap things up, it seems established that visible and infrared lines are formed at different depths in the atmosphere of a Cepheid, and thus in environments in which not only temperature and pressure are different, but also the velocity fields (due to the propagation of the compression wave). The latter is clearly visible in the different behaviour of line asymmetries for optical and infrared lines over the pulsation period (Nardetto et al. 2018, their Fig. 6). Since we measure the line depths directly, without fitting a line profile, we assume that the differences between short- and long-period Cepheids at phases  $\phi \approx 0.0$  we observe in Fig 5 mostly reflect temperature differences rather than uncertainties on measuring line depths related to different line asymmetries.

Furthermore, we note that the theoretical analyses described in Gray (2005) and Jian et al. (2020) are made under the Local Thermodynamical Equilibrium (LTE) assumption, while Vasilyev et al. (2018, 2019) have shown that NLTE effects are important in the atmospheres of Cepheids and maximal at the same phases ( $\phi \approx 0.0$ ) where the discrepancy between optical and NIR line depth ratios is significant.

Finally, it is worth mentioning that long-period Cepheids are known to exhibit cycle-to-cycle variations (e.g., Anderson 2016), including in their line profiles. However, this phenomenon cannot be invoked here since our optical and NIR have been observed simultaneously. Should long-period Cepheids be excluded from the calibration of the LDR, then their  $T_{\text{eff}}$  could not be determined and hence their chemical composition would remain unknown.

## 5 SUMMARY AND CONCLUSION

In the present study, we have derived 87 temperature calibrations, LDR- $T_{\text{eff}}$ , using GIANO high-dispersion near-IR  $H$ -band spectra covering the wavelength range from 14 000 to 16 500 Å that contains numerous atomic lines and molecular bands. The temperatures inferred from the optical spectra obtained in parallel with the HARPS-N spectrograph were adopted as original temperatures to derive calibration relations. The resulting temperature relations are based on 115 spectra of six classical Cepheids.

The calibrations are valid for supergiants with a near-solar metallicity,  $T_{\text{eff}}$  ranging from 4800 to 6500 K and  $M_V$  from  $-3$  to  $-6$  mag. The uncertainties due to the effect of luminosity at temperatures above 6200 K are within 150 K. The typical mean uncertainty per calibration relation is 60–70 K (40–45 K for the most precise ones and 140–160 K for the least precise ones). Using about 60–70 calibrations improves the intrinsic precision to within 30–50 K (for spectra with an S/N of 100–150).

Employing this method, we can derive temperatures of highly reddened objects (such as stars towards the Galactic centre). Adopting these calibrations has already enabled us to determine the temperatures of four Cepheids in the Galactic centre discovered by Matsunaga et al. (2011, 2013, 2015) in order to derive their chemical composition (Kovtyukh et al. 2022). Since many Cepheids have been detected in highly reddened regions, for instance beyond the Galactic center in the far side of the disk (e.g., Feast et al. 2014; Matsunaga et al. 2016; Chen et al. 2018), the newly determined LDR will allow us to derive their chemical composition using NIR spectra. To our knowledge, only Inno et al. (2019) tackled this problem

so far, determining the metallicity of 5 Cepheids candidates in the inner disk by comparing low-resolution ( $R \approx 3000$ ) NIR spectra to a pre-computed grid of synthetic spectra.

Obtaining spectroscopic time-series for a given star would make it possible to track tiny  $T_{\text{eff}}$  variations, potentially related to rotational modulation such as those that have already been detected for dwarf stars – namely, the G8 dwarf  $\xi$  Bootis A (Toner & Gray 1988) and the K0 dwarf  $\sigma$  Dra (Gray et al. 1992). This technique is already being used to study spot activity in giants (Berdugina et al. 2005; Fraska et al. 2005; Frasca et al. 2008). In this respect, hemisphere-averaged temperatures of stars with surface inhomogeneities derived from NIR lines simultaneously to optical lines can be of great help for starspot modelling. Indeed, one expects different average temperatures at different wavelengths due to the wavelength dependence of the contribution of starspots to the total flux.

It would be interesting to search simultaneously for systematic variations in spectral line asymmetries in order to better understand the physics of pulsations in Cepheids. As far as Cepheids are concerned, simultaneous time-series spectroscopy in the optical and infrared domain are crucial to refine our understanding of the Cepheids’ atmosphere dynamics.

In the present paper, the calibration sample is confined to objects with a near-solar metallicity [Fe/H] to circumvent the issue of the dependence of calibrations on [Fe/H]. Investigating such a dependence of calibrations on [Fe/H] will be the goal of further studies.

## 6 DATA AVAILABILITY

This research used the facilities of the Italian Center for Astronomical Archive (IA2) operated by INAF at the Astronomical Observatory of Trieste, programme OPT19A5 (PI: N.Nardetto). The Subaru/IRCS spectra are available at the SMOKA Science Archive <https://smoka.nao.ac.jp/>.

## ACKNOWLEDGEMENTS

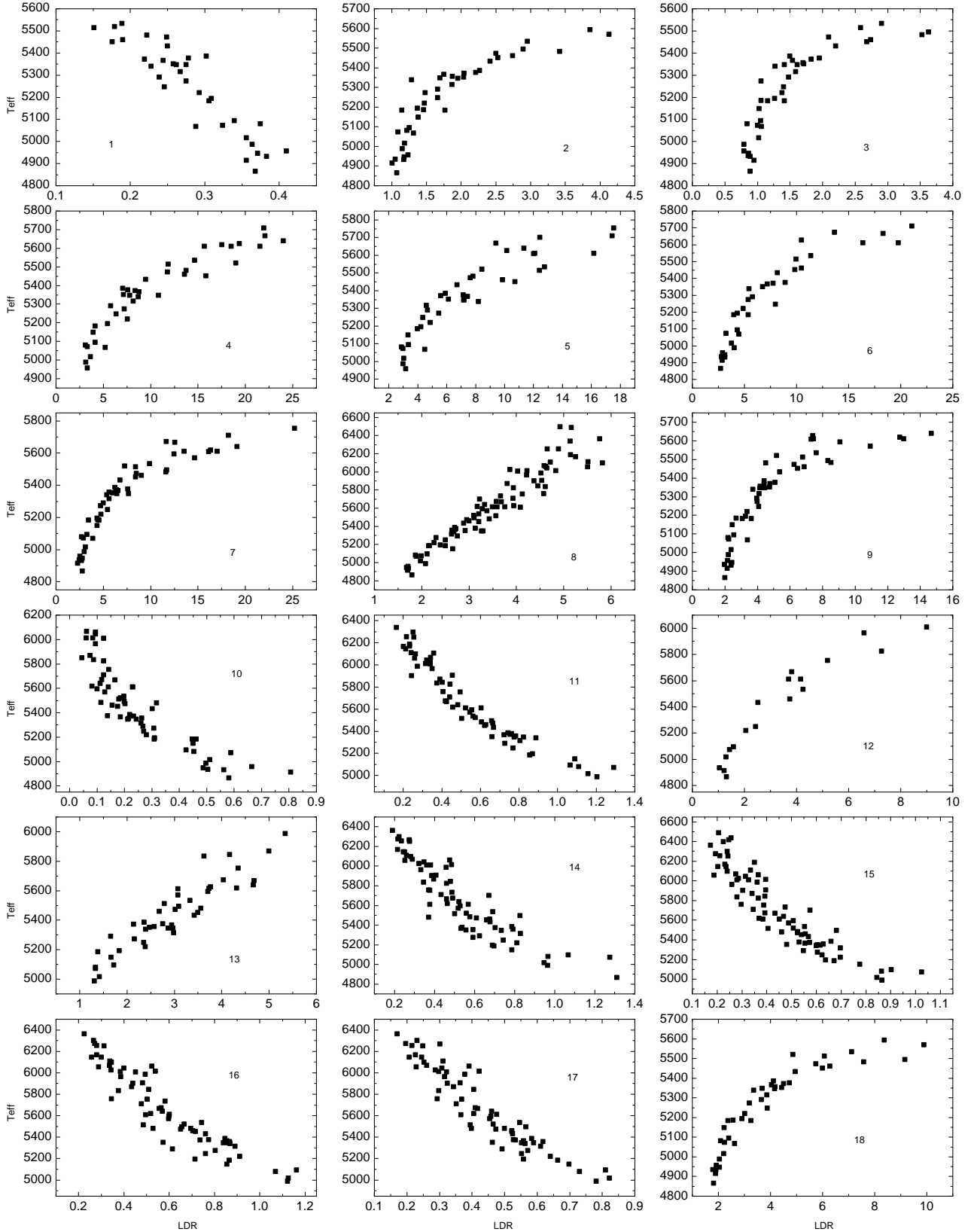
We thank our referee, Dr. Antonio Frasca, for his important comments, which improved our manuscript. VK is grateful to the Vector-Stiftung at Stuttgart, Germany, for support within the program "2022—Immediate help for Ukrainian refugee scientists" under grant P2022-0064.

## REFERENCES

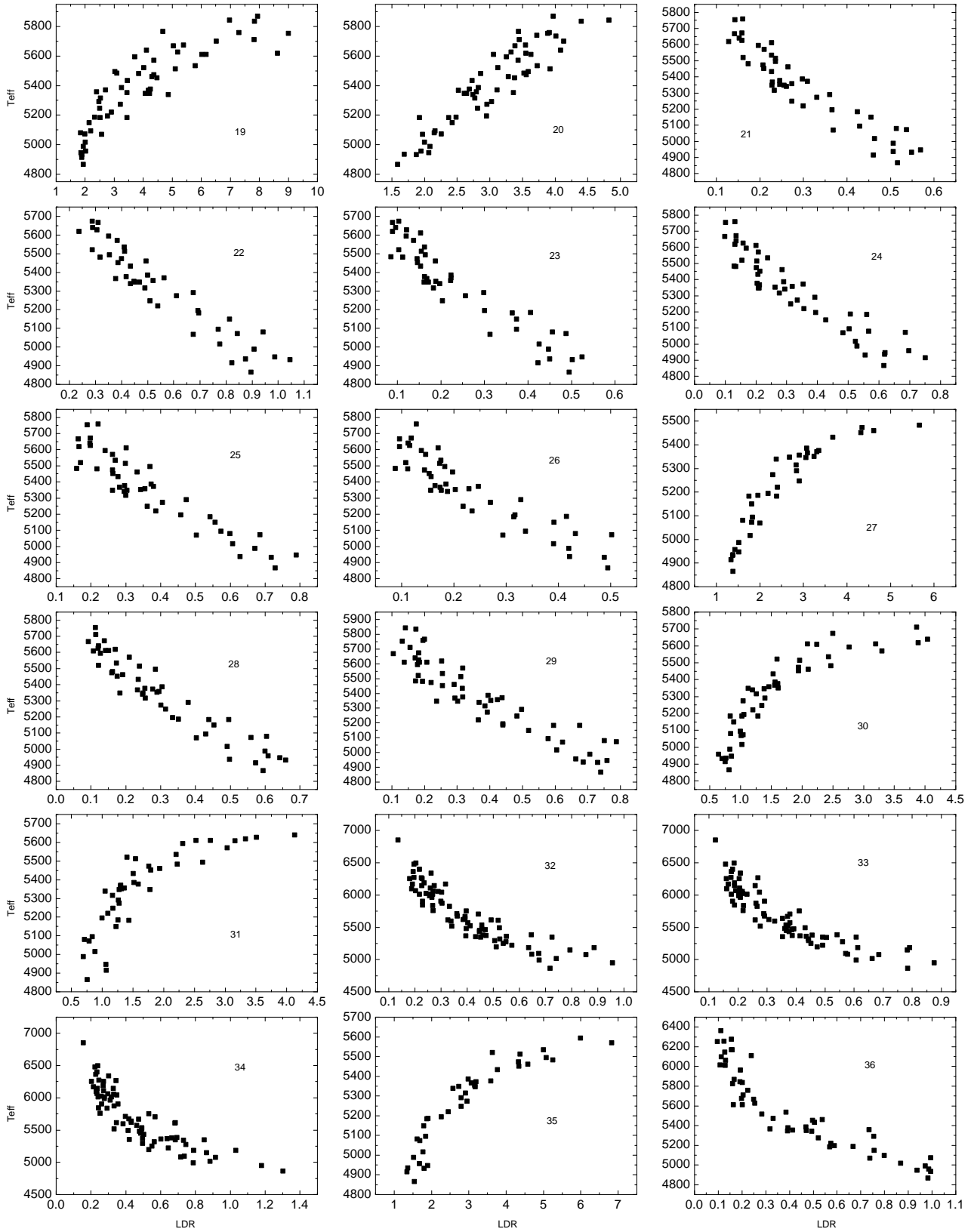
- Afşar M., Bozkurt Z., Topcu G. B., Özdemir S., Sneden Chr., Mace G. N., Jaffe D. T., López-Valdivia R., 2023, ApJ, 949, 86A
- Alonso A., Arribas S., Martínez-Roger C., 1996, A&A, 313, 873
- Anderson R. I., 2016, MNRAS 463, 1707
- Andrievsky S. M., Kovtyukh V. V., Luck R. E., Lepiné J. R. D., Bersier D., Maciel W. J., Barbuy B., Klochkova V.G., Panchuk V. E., Karpischek R. U., 2002a, A&A, 381, 32
- Andrievsky S. M., Bersier D., Kovtyukh V. V., Luck R. E., Maciel W. J., Lepiné J. R. D., Beletsky Yu. V., 2002b, A&A, 384, 140
- Andrievsky S. M., Kovtyukh V. V., Luck R. E., Leépine J. R. D., Maciel W. J., Beletsky Yu. V., 2002c, A&A, 392, 491
- Andrievsky S. M., Luck R. E., Martin P., Leépine J. R. D., 2004, A&A, 413, 159
- Andrievsky S. M., Luck R. E., Kovtyukh V. V., 2005, AJ, 130, 1880
- Berdugina S. V., 2005, Living Rev. Sol. Phys., 2, 8
- Bessell M. S., Castelli F., Plez B., 1998, A&A, 333, 231

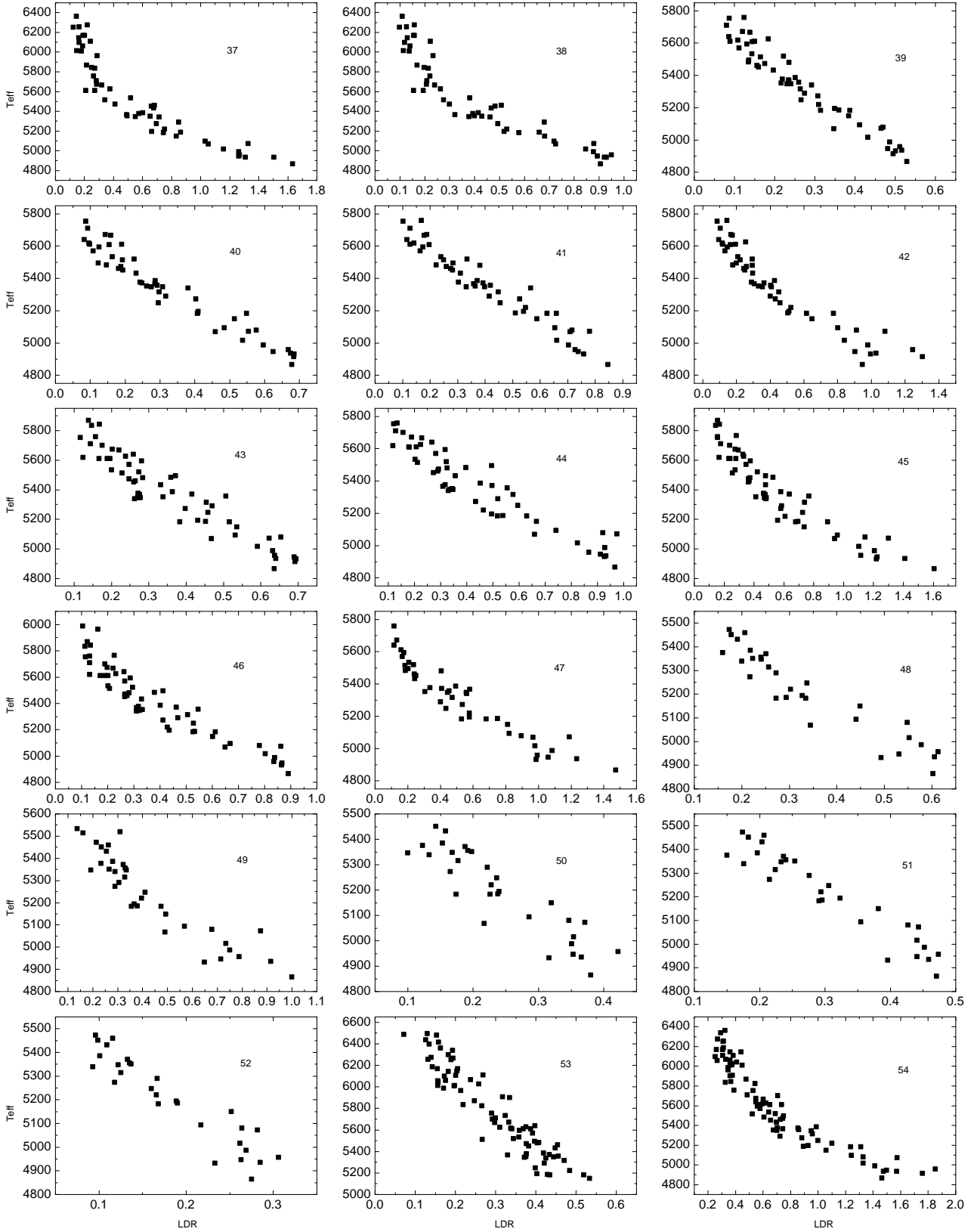
- Biazzo K., Catalano S., Frasca A., Marilli E., 2004, Mem. Soc. Astron. Ital. Supplementi, 5, 109
- Biazzo K., Frasca A., Catalano S., Marilli E., 2006, preprint (arXiv astro-ph/0610584)
- Biazzo K., Frasca A., Catalano S., Marilli E., 2007, Astron. Nachr., 328, 938
- Blackwell D. E., Shallis M. J., 1977, MNRAS, 180, 177
- Caccin B., Penza V., Gomez M. T., 2002, A&A, 386, 286
- Catalano S., Biazzo K., Frasca A., Marilli E., 2002, A&A, 394, 1009
- Cayrel G., Cayrel R., 1963, ApJ, 137, 431
- Chen X., Wang S., Deng L., de Grijs R., Yang M., 2018, ApJS, 237, 28
- Cosentino R. et al., 2012, in McLean I. S., Ramsay S. K., Takami H. eds, Proc. SPIE Conf. Ser. Vol 8446, Ground-based and Airborne Instrumentation for Astronomy IV. SPIE, Bellingham. p. 84461V
- da Silva R. et al., 2016, A&A, 586, A125
- da Silva R. et al., 2022, A&A, 661, A104
- Davis J., Webb R. J., 1974, MNRAS, 168, 163
- Feast M. W., Menzies J. W., Matsunaga N., Whitelock P. A., 2014, Nature, 509, 342
- Frasca A., Biazzo K., Catalano S., Marilli E., Messina S., Rodonò M., 2005, A&A, 432, 647
- Frasca A., Biazzo K., Taş G., Evren S., Lanzafame A. C., 2008, A&A, 479, 557
- Fukue K. et al., 2015, ApJ, 812, 64
- Gehren T., 1981, A&A 100, 97
- Genovali K., et al, 2013, 554, 132
- Genovali K., et al, 2014, 566, 37
- Genovali K., et al, 2015, 580, 17
- Gray D. F., 1989, ApJ 347, 1021
- Gray D. F., Johanson H. L., 1991, PASP 103 439
- Gray, D. F., Baliunas, S. L., Lockwood G. W., Skiff B. A., 1992, ApJ 400, 681
- Gray D. F., 1994, PASP 106, 1248
- Gray D. F., Brown K., 1994, PASP 113, 723
- Gray D. F., The Observation and Analysis of Stellar Photospheres, 2005, 3rd edn., Cambridge Univ. Press, Cambridge, UK
- Hanke M., Hansen C. J., Koch A., Grebel E. K., 2018, A&A, 619, A134
- Inno L. et al., 2019, MNRAS 482, 83
- Jian M., Matsunaga N., Fukue K., 2019, MNRAS, 485, 1310
- Jian M. et al., 2020, MNRAS 494, 1724
- Kobayashi N. et al., 2000, in Iye M., Moorwood A. F.eds, Proc. SPIE Conf. Ser. Vol. 4008, Optical and IR Telescope Instrumentation and Detectors. SPIE, Bellingham. p. 1056
- Kovtyukh V. V., 2007, MNRAS, 378, 617
- Kovtyukh V. V., Andrievsky S. M., 1999, A&A, 351, 597
- Kovtyukh V. et al., 2019, MNRAS, 488, 3211
- Kovtyukh V. V., Gorlova N. I., 2000, A&A, 358, 587
- Kovtyukh V. V., Soubiran C., Belik S. I., Gorlova N. I., 2003, A&A, 411, 559
- Kovtyukh V. V., Andrievsky S. M., Belik S. I., Luck R. E., AJ, 129, 433
- Kovtyukh V. V., Wallerstein G., Andrievsky S. M., 2005, PASP, 117, 1173
- Kovtyukh V. V., Wallerstein G., Andrievsky S. M., 2005, PASP, 117, 1182
- Kovtyukh V. V., Soubiran C., Bienaymé O., Mishenina T. V., Belik S. I., 2006, MNRAS, 371, 879
- Kovtyukh V. et al., 2016, MNRAS, 460, 2077
- Kovtyukh V. et al., 2018a, PASP, 130, 54201
- Kovtyukh V., Yegorova I., Andrievsky S., Korotin S., Saviane I., Lemasle B., Chekhonadskikh F., Belik S., 2018b, MNRAS, 477, 2276
- Kovtyukh V. et al., 2019, MNRAS, 488, 3211
- Kovtyukh V. V., Korotin S. A., Andrievsky S. M., Matsunaga N., Fukue K., 2022, MNRAS, 516, 4269
- Lemasle B., François P., Bono G., Mottini M., Primas F., Romaniello M., 2007, A&A, 467, 283
- Lemasle B., François P., Piersimoni A., Pedicelli S., Bono G., Laney C. D., Primas F., Romaniello M., 2008, A&A , 490, 613
- Lemasle B. et al., 2013, A&A, 558, A31
- Lemasle B. et al., 2015, A&A , 579, A47
- Lemasle B. et al., 2017, A&A, 608, A85
- Lemasle B. et al., 2018, A&A, 618, A160
- Lemasle B. , Hanke M., Storm J., Bono G., Grebel E. K., 2020, A&A, 641, A71
- Luck R. E., 2018, AJ, 156, 171
- Luck R. E., Lambert D. L., 2011, AJ, 142, 136
- Luck R. E., Andrievsky S. M., 2004, AJ, 128, 343
- Luck R. E. , Gieren W. P., Andrievsky S. M., Kovtyukh V. V., Fouqué P., Pont F., Kienzle F., 2003, A&A, 401, 939
- Luck R. E. , Kovtyukh V. V., Andrievsky S. M., 2006, AJ, 132, 902
- Luck R. E., Andrievsky S. M., Fokin A., Kovtyukh V. V., 2008, AJ, 136, 98
- Luck R. E., Andrievsky S. M., Kovtyukh V. V., Gieren W., Graczyk D., 2011, AJ, 142, 51
- Martin R. P., Andrievsky S. M., Kovtyukh V . V ., Korotin S. A., Yegorova I. A., Saviane I., 2015, MNRAS, 449, 4071
- Matsunaga N., Kawadu T., Nishiyama Sh., Nagayama T., Kobayashi N., Tamura M., Bono G., Feast M. W., Nagata T., 2011, Nature, 477, Iss. 7363, 188
- Matsunaga N., Feast M. W., Kawadu T., Nishiyama Sh., Nagayama T., Nagata T., Tamura M., Bono G., Kobayashi N., 2013, MNRAS 429, 385
- Matsunaga N., Fukue K., Yamamoto R., Kobayashi N., Inno L., Genovali K., Bono G., et al., 2015, ApJ, 799, 46
- Matsunaga N., Feast M. W., Bono G., Kobayashi N., Inno L., Nagayama T., Nishiyama S., et al., 2016, MNRAS, 462, 414.
- Matsunaga N., 2017, in European Physical Journal Web of Conferences, 152, p.01007 preprint ( arXiv:1705.02547 )
- Matsunaga N., Jian M., Taniguchi D., Elgueta S. S., 2021, MNRAS 506, 1031
- Nardetto N., Mourard D., Kervella P., Mathias P., Mérand A., Bersier D., 2006, A&A, 453, 309
- Nardetto N., Mourard D., Mathias P., Fokin A., Gillet D., 2007, A&A, 471, 661
- Nardetto N., Stoekl A., Bersier D., Barnes T. G., 2008a, A&A, 489, 1255
- Nardetto N., Groh J. H., Kraus S., Millour F., Gillet D., 2008b, A&A, 489, 1263
- Nardetto N. et al., 2018, A&A, 616, A92
- Nardetto N. et al., 2023, A&A , 671, A14
- Ness M., Hogg D. W., Rix H. W., Ho A. Y. Q., Zasowski G., 2015, ApJ, 808, 16
- Ortigia L. et al., 2014, in Ramsay S. K., McLean I. S., Takami H. eds, Proc. SPIE Conf. Ser. Vol. 9147, Ground-based and Airborne Instrumentation for Astronomy V. SPIE, Bellingham. p. 91471E
- Pedicelli S. et al., 2010, A&A, 518, A11
- Proxauf B. et al., 2018, A&A, 616, A82
- Recio-Blanco A., Bijaoui A., Laverny P., 2006, MNRAS, 370, 141
- Romaniello M. et al., 2008, A&A, 488, 731
- Romaniello M. et al., 2022, A&A, 658, A29
- Strassmeier K. G., Schordan P., 2000, Astron. Nachr., 321, 277
- Taniguchi D. et al., 2018, MNRAS, 473, 4993
- Taniguchi D. et al., 2021, MNRAS, 502, 4210
- Toner C. G., Gray D. F., 1988, ApJ 334, 1008
- van Hoof A. Struve O., 1953, PASP 65, 158
- Vasilyev V. Ludwig H.-G. Freytag B. Lemasle B. Marconi M., 2017, A&A, 606, 140
- Vasilyev V., Ludwig H. -G., Freytag B., Lemasle B., Marconi M., A&A 611, 19
- Vasilyev V., Amarsi A. M., Ludwig, H. -G., Lemasle B., A&A 624, 85

## APPENDIX A: CALIBRATIONS

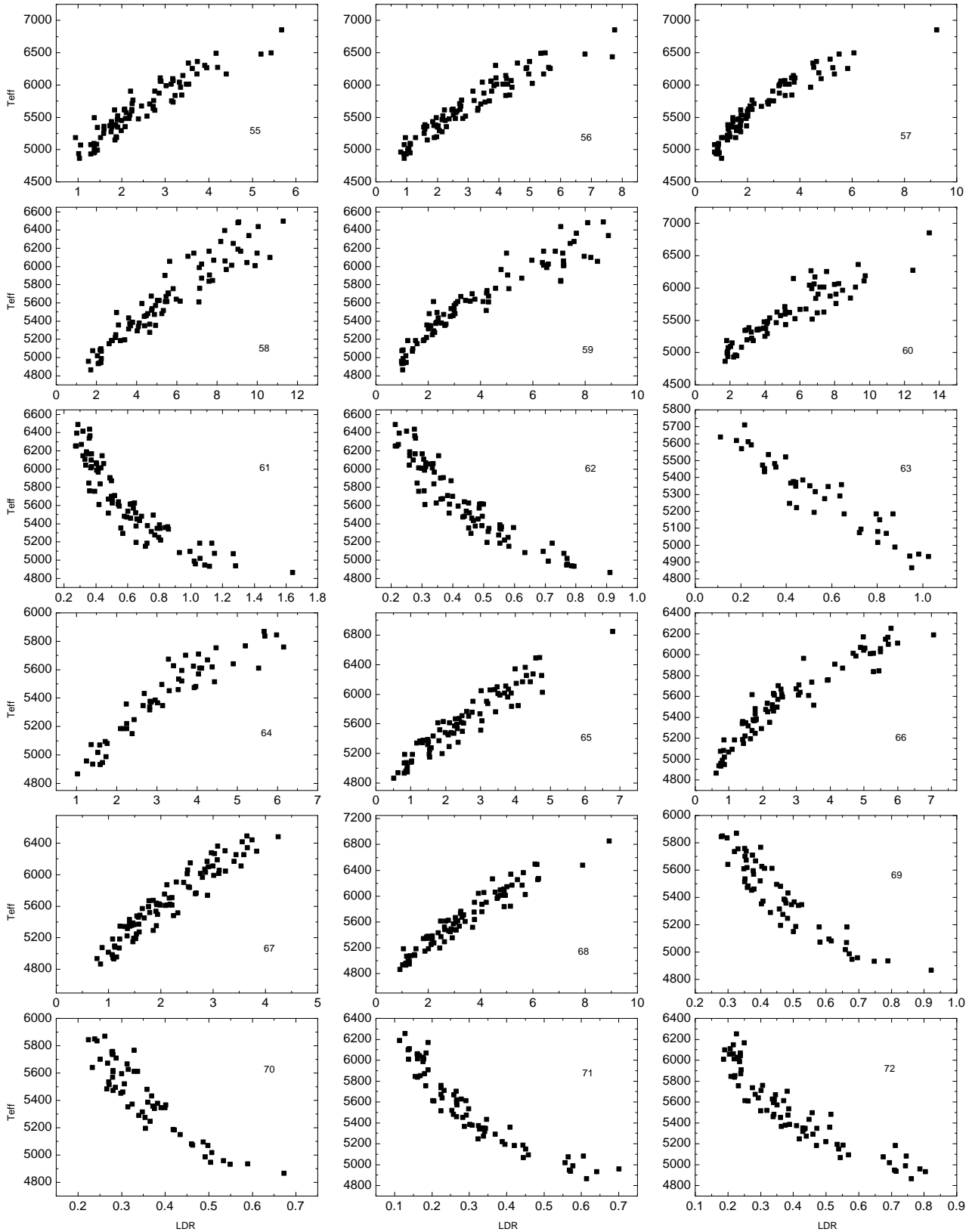


**Figure A1.** Calibration relations 1-18, showing the variation of  $T_{\text{eff}}$  as a function of the line depth ratio (LDR).

**Figure A2.** Same as in Fig A1 but for calibration relations 19-36



**Figure A3.** Same as in Fig A1 but for calibration relations 37-54

**Figure A4.** Same as in Fig A1 but for calibration relations 55-72

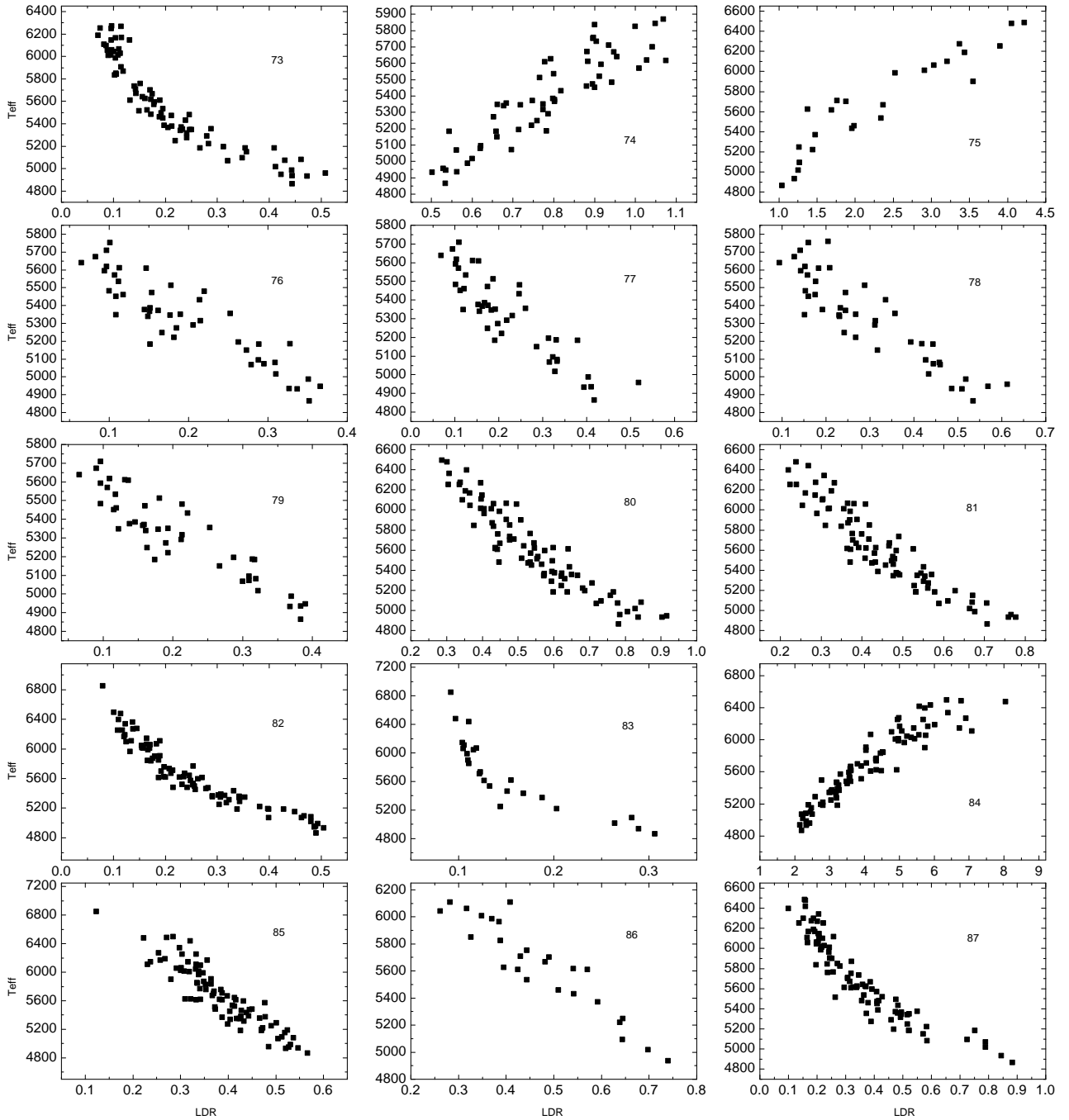


**Figure A5.** Same as in Fig A1 but for calibration relations 73-87

Table A1: Individual  $T_{\text{eff}}$  determinations for calibrating Cepheids. For each individual spectrum, the table provides the observing log, including the pulsation phase of the Cepheid, the temperature and its associated uncertainty, the number of calibrations used for both the calibrating (optical) HARPS-N spectra and the near-infrared GIANO spectra.

Cep	UT Date	UT	JD	phase	GIANO				HARPS-N			
					$T_{\text{eff}}$ (K)	$\sigma$ (K)	N	$\sigma/\sqrt{N}$ (K)	$T_{\text{eff}}$ (K)	$\sigma$ (K)	N	$\sigma/\sqrt{N}$ (K)
$\delta$ Cep	2019-07-14	03-06-55	58678.62980	.087	6219	103	16	25.7	6361	54	67	6.6
$\delta$ Cep	2019-07-15	04-30-38	58679.68793	.284	5847	76	35	12.9	5869	65	79	7.3
$\delta$ Cep	2019-07-16	04-39-15	58680.69392	.471	5644	88	49	12.6	5618	71	81	7.9
$\delta$ Cep	2019-07-17	02-17-24	58681.59541	.639	5537	95	68	11.5	5482	46	76	5.2
$\delta$ Cep	2019-07-18	02-38-33	58682.61010	.828	5612	102	43	15.6	5738	73	79	8.2
$\delta$ Cep	2019-07-19	04-30-31	58683.68785	.029	6295	87	12	25.0	6486	60	65	7.4
$\delta$ Cep	2019-08-08	03-57-43	58703.66508	.752	5513	84	66	10.4	5520	46	69	5.5
$\delta$ Cep	2019-08-18	04-54-54	58713.70479	.623	5436	127	59	16.6	5494	61	77	7.0
$\delta$ Cep	2019-08-21	02-23-57	58716.59996	.162	6098	137	26	26.8	6145	68	74	7.9
$\delta$ Cep	2019-08-23	00-41-51	58718.52906	.522	5548	73	59	9.4	5570	59	77	6.8
$\delta$ Cep	2019-08-25	00-31-23	58720.52179	.893	6000	212	17	51.5	6115	91	74	10.6
$\delta$ Cep	2019-08-26	05-07-52	58721.71379	.115	6197	120	24	24.5	6273	63	68	7.6
$\delta$ Cep	2019-09-08	00-07-51	58734.50545	.499	5559	81	60	10.4	5593	70	77	7.9
$\delta$ Cep	2019-09-10	02-48-54	58736.61729	.893	...	...	...	...	6139	111	74	12.9
$\delta$ Cep	2019-09-10	21-51-31	58737.41077	.041	6423	129	15	33.2	6478			
$\delta$ Cep	2019-09-13	00-10-54	58739.50756	.431	5642	91	51	12.7	5639	82	80	9.2
$\delta$ Cep	2019-09-21	00-46-38	58747.53238	.927	6120	97	18	22.9	6339	63	67	7.7
S Sge	2019-04-27	05:26:53	58600.72700	.519	5474	68	79	7.7	5460	107	71	12.7
S Sge	2019-04-28	05:20:20	58601.72245	.638	5314	74	82	8.1	5247	143	57	18.9
S Sge	2019-05-03	05:23:26	58606.72460	.235	5942	113	33	19.7	5986	105	76	12.1
S Sge	2019-05-04	05:13:11	58607.71748	.353	5704	81	45	12.1	5709	135	80	15.1
S Sge	2019-05-05	05:08:59	58608.71457	.472	5529	74	73	8.7	5534	135	73	15.8
S Sge	2019-05-06	05:12:32	58609.71703	.592	5355	72	84	7.9	5371	142	69	17.1
S Sge	2019-05-08	05:34:49	58611.73251	.832	5779	99	15	25.4	5825	122	44	18.5
S Sge	2019-05-09	05:30:37	58612.72959	.951	6221	173	26	33.9	6186	125	70	15.0
S Sge	2019-05-10	05:07:57	58613.71385	.069	6130	127	33	22.0	6098	138	68	16.7
S Sge	2019-05-17	03:44:34	58620.65594	.897	5898	185	28	35.0	5901	151	68	18.3
S Sge	2019-05-18	03:14:19	58621.63494	.014	6204	142	28	26.8	6250	149	56	19.9
S Sge	2019-05-19	03:05:31	58622.62883	.132	6013	106	35	17.9	6011	117	66	14.4
S Sge	2019-05-20	03:39:47	58623.65262	.255	6018	152	33	26.5	6013	134	78	15.2
S Sge	2019-05-21	03:36:57	58624.65065	.374	5666	76	46	11.3	5672	110	69	13.2
S Sge	2019-05-22	03:35:59	58625.64998	.493	5492	53	75	6.1	5451	130	77	14.8
S Sge	2019-05-23	03:09:11	58626.63137	.610	5290	66	77	7.5	5356	143	65	17.8
S Sge	2019-05-24	03:45:09	58627.65635	.732	5354	67	80	7.5	5385	143	62	18.2
S Sge	2019-06-07	02:57:32	58641.62328	.398	5578	113	50	16.0	5611	105	81	11.6
S Sge	2019-06-09	02:38:55	58643.61035	.636	5322	60	75	6.9	5315	141	69	17.0
S Sge	2019-06-11	02:09:16	58645.58976	.872	5823	105	31	18.9	5905	136	63	17.1
S Sge	2019-06-13	01:13:25	58647.55098	.106	5964	129	36	21.5	6060	147	70	17.6
S Sge	2019-06-20	00:30:13	58654.52098	.937	6026	200	31	35.9	6055	153	66	18.9
S Sge	2019-08-08	03:37:25	58703.65098	.798	5492	170	59	22.2	5480	183	47	26.6
S Sge	2019-08-18	22:30:19	58714.43771	.085	6001	111	30	20.3	6067	123	77	14.0
S Sge	2019-09-07	22:21:46	58734.43178	.471	5496	66	74	7.6	5472	78	73	9.2
S Sge	2019-09-18	23:51:33	58745.49413	.790	5555	129	41	20.1	5626	154	58	20.2
T Vul	2018-08-09	23-17-25	58340.47042	.534	5573	167	39	26.7	5611	146	52	20.2
T Vul	2018-08-15	20-53-51	58346.37072	.864	6191	105	9	35.0	6299	157	37	25.8
T Vul	2018-08-17	23-15-26	58348.46905	.337	5763	133	32	23.5	5753	124	66	15.3
T Vul	2018-08-24	21-01-38	58355.37613	.894	6325	267	11	80.6	6436	125	41	19.4
T Vul	2018-08-25	00-46-59	58355.53262	.929	6330	182	13	50.5	6395	146	53	20.1
T Vul	2018-08-25	20-49-05	58356.36741	.118	6065	147	22	31.3	6144	137	70	16.3
T Vul	2018-08-26	02-18-48	58356.59638	.169	5997	143	32	25.2	6043	137	54	18.7
T Vul	2018-08-29	01-41-14	58359.57030	.840	6049	211	20	47.2	6107	143	53	19.7

Table A1: continued.

Cep	UT Date	UT	JD	phase	GIANO				HARPN			
					$T_{\text{eff}}$ (K)	$\sigma$ (K)	N	$\sigma/\sqrt{N}$ (K)	$T_{\text{eff}}$ (K)	$\sigma$ (K)	N	$\sigma/\sqrt{N}$ (K)
T Vul	2018-09-07	01-42-29	58368.57116	.869	6083	161	22	34.3	6267	155	58	20.3
T Vul	2018-09-10	20-25-15	58372.35086	.721	5638	216	22	46.0	5625	124	55	16.7
T Vul	2018-09-12	00-55-50	58373.53877	.989	6306	146	13	40.4	6495	177	48	25.5
T Vul	2018-09-12	02-57-19	58373.62313	.008	6096	198	5	88.6	6297	138	55	18.6
T Vul	2018-10-01	00-07-06	58392.50493	.265	5898	126	10	39.9	5850	113	79	12.8
T Vul	2018-12-10	19-15-42	58463.30256	.227	...	...	...	...	5852	149	68	18.0
T Vul	2018-12-20	19-22-38	58473.30738	.482	5599	229	19	52.6	5615	160	57	21.2
T Vul	2019-08-08	03-27-40	58703.64421	.413	5681	178	52	24.7	5609	140	60	18.1
T Vul	2019-08-16	20-41-57	58712.36246	.379	5712	139	26	27.3	5734	142	78	16.0
T Vul	2019-09-08	01-13-05	58734.55075	.381	5634	123	37	20.1	5700	134	61	17.1
T Vul	2019-09-10	20-07-42	58737.33868	.010	6362	235	10	74.4	6415	151	63	19.0
X Cyg	2019-04-27	05-10-08	58600.71537	.360	5108	40	81	4.4	5094	114	60	14.7
X Cyg	2019-04-28	05-32-30	58601.73090	.422	5047	56	78	6.3	5016	90	70	10.8
X Cyg	2019-05-01	05-37-25	58604.73431	.605	4931	63	18	14.8	4865	90	52	12.5
X Cyg	2019-05-03	05-13-56	58606.71800	.726	5191	143	69	17.2	5183	112	41	17.6
X Cyg	2019-05-04	04-58-11	58607.70707	.787	5416	97	79	10.9	5366	78	59	10.2
X Cyg	2019-05-05	04-54-06	58608.70423	.848	5418	68	81	7.6	5376	77	67	9.4
X Cyg	2019-05-06	04-57-28	58609.70657	.909	5973	111	31	20.0	6008	141	80	15.8
X Cyg	2019-05-10	05-18-49	58613.72140	.154	5400	71	83	7.8	5432	124	74	14.5
X Cyg	2019-05-17	03-30-41	58620.64630	.576	...	...	...	...	4851	76	57	10.0
X Cyg	2019-05-18	03-56-20	58621.66412	.638	...	...	...	...	4913	97	55	13.1
X Cyg	2019-05-19	03-15-30	58622.63576	.698	5126	86	64	10.7	5068	130	57	17.2
X Cyg	2019-05-20	03-29-31	58623.64549	.759	5333	94	73	11.0	5339	104	53	14.3
X Cyg	2019-05-21	03-26-24	58624.64333	.820	5373	89	79	10.0	5346	72	60	9.3
X Cyg	2019-05-22	03-20-50	58625.63946	.881	5638	99	50	14.0	5667	73	80	8.2
X Cyg	2019-05-23	02-59-07	58626.62438	.941	6058	127	24	25.8	6109	137	72	16.1
X Cyg	2019-05-24	03-24-59	58627.64234	.003	5944	132	34	22.6	5963	117	79	13.1
X Cyg	2019-06-06	04-54-08	58640.70425	.800	5368	91	80	10.2	5347	78	61	9.9
X Cyg	2019-08-08	03-46-45	58703.65746	.642	...	...	...	...	4924	111	55	15.0
X Cyg	2019-08-22	02-45-33	58717.61496	.494	4944	46	39	7.4	4935	84	67	10.3
X Cyg	2019-09-07	23-41-56	58734.48745	.524	4933	67	12	19.4	4914	97	65	12.0
X Cyg	2019-09-19	23-41-13	58746.48695	.256	5265	51	73	5.9	5220	72	72	8.5
SV Vul	2019-04-27	04:52:25	58600.70306	.139	5967	150	35	25.4	5843	139	73	16.2
SV Vul	2019-04-28	05:10:03	58601.71531	.161	5862	134	36	22.4	5758	137	81	15.2
SV Vul	2019-05-01	05:09:53	58604.71519	.228	5599	137	70	16.4	5513	141	77	16.1
SV Vul	2019-05-04	05:22:10	58607.72372	.295	5431	91	81	10.2	5351	109	72	12.9
SV Vul	2019-05-17	03:53:28	58620.66212	.583	5049	71	73	8.4	5080	84	61	10.7
SV Vul	2019-05-21	03:47:34	58624.65803	.672	5003	89	69	10.7	4987	97	69	11.7
SV Vul	2019-06-07	03:06:45	58641.62968	.051	6133	136	26	26.7	6167	131	67	16.0
SV Vul	2019-06-11	00:58:23	58645.54054	.138	5937	109	36	18.1	5834	125	71	14.8
SV Vul	2019-06-20	01:29:58	58654.56247	.339	5327	113	81	12.5	5290	119	74	13.9
SV Vul	2019-07-15	03:16:09	58679.63621	.897	5323	93	78	10.5	5273	96	55	12.9
SV Vul	2019-07-18	03:27:34	58682.64414	.964	6121	145	25	29.0	6166	88	52	12.2
SV Vul	2019-08-08	03:17:46	58703.63733	.432	5204	105	78	11.9	5185	113	71	13.4
SV Vul	2019-08-09	21:23:23	58705.39123	.471	5153	90	80	10.1	5149	118	69	14.2
SV Vul	2019-08-18	22:21:18	58714.43145	.672	4979	105	46	15.4	4946	109	57	14.5
SV Vul	2019-08-21	01:27:25	58716.56070	.720	4968	102	46	15.0	4932	146	40	23.0
SV Vul	2019-08-22	20:51:45	58718.36927	.760	4937	107	65	13.3	4957	149	31	26.8
SV Vul	2019-08-25	02:36:38	58720.60877	.810	...	...	...	...	4983	140	39	22.5
SV Vul	2019-08-27	20:46:13	58723.36542	.871	5137	82	62	10.4	5183	167	48	24.1
SV Vul	2019-08-30	20:20:17	58726.34741	.938	5698	137	14	36.6	5766	138	52	19.2
SV Vul	2019-09-03	20:30:20	58730.35439	.027	6257	158	24	32.3	6253	117	62	14.8
SV Vul	2019-09-07	20:35:19	58734.35785	.116	6034	135	26	26.4	6026	160	42	24.7
SV Vul	2019-09-19	23:32:17	58746.48075	.386	5267	89	81	9.9	5194	137	70	16.4

Table A1: continued.

Cep	UT Date	UT	JD	phase	GIANO				HARPN			
					$T_{\text{eff}}$ (K)	$\sigma$ (K)	N	$\sigma/\sqrt{N}$ (K)	$T_{\text{eff}}$ (K)	$\sigma$ (K)	N	$\sigma/\sqrt{N}$ (K)
S Vul	2019-04-27	04:11:07	58600.67438	.792	5282	89	72	10.5	5223	119	60	15.4
S Vul	2019-05-06	05:22:17	58609.72380	.925	5856	154	35	26.1	5773	112	47	16.3
S Vul	2019-05-10	04:43:10	58613.79664	.985	5990	163	32	28.7	5971	121	56	16.2
S Vul	2019-05-18	03:29:57	58621.64579	.101	6069	117	33	20.4	5891	132	72	15.5
S Vul	2019-05-24	03:55:57	58627.66385	.189	5900	142	35	24.0	5748	134	80	15.0
S Vul	2019-06-06	05:05:16	58640.71199	.381	5478	136	74	15.9	5438	139	75	16.1
S Vul	2019-07-14	02:58:45	58678.62413	.938	5822	157	32	27.8	5779	152	42	23.5
S Vul	2019-07-19	04:19:23	58683.68012	.012	5965	145	33	25.2	5980	155	54	21.1
S Vul	2019-09-03	21:22:41	58730.39075	.699	5201	79	79	8.9	5160	123	70	14.7
S Vul	2019-09-18	23:28:46	58745.47831	.920	5548	139	43	21.1	5566	135	53	18.5

Table A2: LDR- $T_{\text{eff}}$  calibration relations. For each relation, the wavelengths of both lines and the corresponding chemical element are provided, together with the analytic function type, the value of the coefficients, the average accuracy of the calibration and the temperature range wherein it can be used. When one of the lines is blended, representing two or more elements, only the elements which predominantly contribute to the blend are indicated.

N	Lambda1 (Å)	El 1	Lambda2 (Å)	El 2	Name	$T_{\text{eff}} =$	sigma (K)	$T_{\text{eff}}$ (K)	a	b	c	d
1	14968.327	Fe I	15024.992	Mg I	Quadratic Fit	$a+br+cr^2$	81	4800–5550	5664.6	-115.54	-4632.1	...
2	14968.327	Fe I	15317.843	Ti I	Modified Exponential	$a \cdot b^{1/r}$	70	4950–5550	5831.4	-0.17068	...	...
3	15017.700	Fe I	15317.843	Ti I	Modified Hoerl Model	$ab^{1/r}c$	66	4900–5550	6022.1	0.84430	-0.032450	...
4	15024.992	Mg I	15221.551	Ni I	Logarithm Fit	$a+b\ln(r)$	56	4950–5700	4662.1	320.08	...	...
5	15024.992	Mg I	15328.367	Sc I	Modified Hoerl Model	$ab^{1/r}c$	71	5000–5650	5079.3	0.84156	0.044211	...
6	15040.246	Mg I+	15317.843	Ti I	Hoerl Model	$a(b')^c(r^e)$	62	4800–5650	4431.1	0.99541	0.11299	...
7	15047.705	Mg I	15317.843	Ti I	Modified Hoerl Model	$ab^{1/r}c$	54	4800–5650	5263.3	0.78937	0.030078	...
8	15047.705	Mg I	15387.803	Fe I	Linear Fit	$a+br$	124	5000–6250	4367.8	354.19	...	...
9	15051.749	Fe I	15317.843	Ti I	Modified Exponential	$ae^{b/r}$	61	4850–5600	5769.8	-0.32729	...	...
10	15063.513	Mg I	15403.791	S I	Shifted Power Fit	$a(r-b)^c$	130	4900–5900	4738.9	-0.050804	-0.10471	...
11	15077.287	Fe I	15422.276	S I	Quadratic Fit	$a+br+cr^2$	81	5100–6350	6713.5	-2587.1	1006.5	...
12	15094.695	Fe I	15317.843	Ti I	Logarithm Fit	$a+b\ln(r)$	74	4800–6000	4843.3	537.54	...	...
13	15178.422	V I+Cr I	15210.356	Sc I?	Linear Fit	$a+br$	90	5000–5950	4816.9	208.72	...	...
14	15178.422	V I+Cr I	15403.791	S I	Logarithm Fit	$a+b\ln(r)$	144	4950–6350	5100.0	-775.93	...	...
15	15178.422	V I+Cr I	15422.276	S I	Modified Hoerl Model	$ab^{1/r}c$	140	5000–6500	4992.1	0.99911	-0.15195	...
16	15178.422	V I+Cr I	15469.816	S I	Logarithm Fit	$a+b\ln(r)$	126	5100–6300	5162.0	-826.02	...	...
17	15178.422	V I+Cr I	15478.482	S I+Fe I	Quadratic Fit	$a+br+cr^2$	122	5100–6300	7008.1	-3996.6	1901.3	...
18	15207.526	Fe I	15317.843	Ti I	Modified Exponential	$ae^{b/r}$	46	4850–5550	5730.2	-0.27878	...	...
19	15207.526	Fe I	15328.367	Sc I	Modified Exponential	$ae^{b/r}$	105	4950–5700	5980.2	-0.34844	...	...
20	15207.526	Fe I	15490.882	Fe I?	Quadratic Fit	$a+br+cr^2$	100	4800–5750	3954.0	639.38	-50.183	...
21	15210.356	Sc I?	15217.777	Mn I	Quadratic Fit	$a+br+cr^2$	81	4950–5650	6091.5	-3312.0	2270.0	...
22	15210.356	Sc I?	15224.729	Fe I	Quadratic Fit	$a+br+cr^2$	75	4950–5600	6041.5	-1678.75	569.95	...
23	15210.356	Sc I?	15376.831	S I	Quadratic Fit	$a+br+cr^2$	76	4950–5600	5827.4	-2602.4	1730.0	...
24	15210.356	Sc I?	15400.077	S I	Quadratic Fit	$a+br+cr^2$	82	4950–5600	5884.8	-2216.1	1247.7	...
25	15210.356	Sc I?	15531.752	Fe I	Quadratic Fit	$a+br+cr^2$	89	4950–5600	5932.8	-1868.3	695.06	...
26	15210.356	Sc I?	15686.441	Fe I	Quadratic Fit	$a+br+cr^2$	92	5000–5600	5882.1	-2908.7	2148.0	...
27	15219.618	Fe I	15317.843	Ti I	Modified Exponential	$ae^{(b/r)}$	58	4900–5450	5721.2	-0.20768	...	...
28	15221.551	Ni I	15376.831	S I	Quadratic Fit	$a+br+cr^2$	74	4950–5650	5885.8	-2320.8	1317.5	...
29	15221.551	Ni I	15400.077	S I	Quadratic Fit	$a+br+cr^2$	94	4950–5750	5953.6	-1965.9	893.11	...
30	15224.729	Fe I	15317.843	Ti I	Modified Exponential	$ae^{b/r}$	75	4950–5600	5836.2	-0.12437	...	...
31	15239.712	Fe I	15317.843	Ti I	Modified Exponential	$ae^{b/r}$	96	5000–5600	5811.4	-0.11757	...	...
32	15239.712	Fe I	15403.791	S I	Hoerl Model	$a(b')^c(r^e)$	149	5050–6900	4446.5	1.1119	-0.20245	...
33	15239.712	Fe I	15422.276	S I	Modified Hoerl Model	$ab^{1/r}c$	157	5050–6900	4792.2	1.0139	-0.10608	...
34	15239.712	Fe I	15469.816	S I	Modified Hoerl Model	$ab^{1/r}c$	180	5000–6900	5003.7	0.99900	-0.15005	...
35	15244.974	Fe I	15317.843	Ti I	Modified Exponential	$ae^{b/r}$	60	4900–5550	5766.7	-0.23036	...	...
36	15284.242	Ti I	15422.276	S I	Modified Hoerl Model	$ab^{1/r}c$	132	5000–6200	4975.6	0.99943	-0.10023	...
37	15284.242	Ti I	15469.816	S I	Modified Hoerl Model	$ab^{1/r}c$	140	4850–6250	5105.0	0.99942	-0.10170	...
38	15284.242	Ti I	15478.482	S I+Fe I	Logarithm Fit	$a+b\ln(r)$	130	4900–6200	4897.0	-585.43	...	...
39	15317.843	Ti I	15335.383	Fe I	Quadratic Fit	$a+br+cr^2$	62	4800–5700	5877.0	-2324.2	951.69	...
40	15317.843	Ti I	15376.831	S I	Quadratic Fit	$a+br+cr^2$	59	4950–5650	5806.8	-1748.5	677.34	...
41	15317.843	Ti I	15400.077	S I	Quadratic Fit	$a+br+cr^2$	61	4950–5650	5820.4	-1236.2	188.60	...
42	15317.843	Ti I	15403.791	S I	Shifted Power Fit	$a(r-b)^c$	63	4950–5700	5077.1	-0.20476	-0.097246	...
43	15328.367	Sc I	15376.831	S I	Quadratic Fit	$a+br+cr^2$	92	4950–5750	5999.2	-2046.8	743.43	...
44	15328.367	Sc I	15422.276	S I	Quadratic Fit	$a+br+cr^2$	79	4950–5650	5868.9	-1414.2	487.91	...
45	15328.367	Sc I	15469.816	S I	Shifted Power Fit	$a(r-b)^c$	75	4800–5800	5188.3	-0.20991	-0.10800	...
46	15328.367	Sc I	15478.482	S I+Fe I	Modified Hoerl Model	$ab^{1/r}c$	122	5000–5900	4950.2	0.99952	-0.081113	...
47	15363.530	Ni I?	15469.816	S I	Hoerl Model	$a(b')^c(r^e)$	61	4900–5650	5305.5	0.94907	-0.033075	...
48	15373.395	V I?	15422.276	S I	Power Fit	$ar^b$	59	4950–5450	4762.4	-0.076892	...	...
49	15373.395	V I?	15469.816	S I	Quadratic Fit	$a+br+cr^2$	67	4950–5500	5753.4	-1630.6	804.19	...
50	15373.395	V I?	15591.490	Fe I	Linear Fit	$a+br$	75	4900–5400	5604.3	-1695.0	...	...
51	15373.395	V I?	15604.221	Fe I	Linear Fit	$a+br$	58	4900–5450	5712.6	-1637.6	...	...
52	15373.395	V I?	15748.988	Mg I	Linear Fit	$a+br$	66	4900–5400	5653.2	-2445.6	...	...
53	15381.960	Fe I	15422.276	S I	Quadratic Fit	$a+br+cr^2$	135	5100–6600	6901.6	-4616.3	2415.2	...
54	15387.803	Fe I	15403.791	S I	3rd degree Polynom. Fit	$a+br+cr^2+dr^3$	111	4900–6350	6954.8	-3223.0	1889.5	-404.99

Table A2: continued.

N	Lambda1 (Å)	El 1	Lambda2 (Å)	El 2	Name	$T_{\text{eff}} =$	sigma (K)	$T_{\text{eff}}$ (K)	a	b	c	d
55	15400.077	S <sub>1</sub>	15490.882	Fe <sub>1?</sub>	Quadratic Fit	a+br+cr <sup>2</sup>	145	4700–6900	4316.8	654.34	-42.104	...
56	15403.791	S <sub>1</sub>	15490.882	Fe <sub>1?</sub>	Quadratic Fit	a+br+cr <sup>2</sup>	122	4700–6900	4602.7	434.24	-22.149	...
57	15403.791	S <sub>1</sub>	15665.241	Fe <sub>1</sub>	Modified Hoerl Model	ab <sup>1/r</sup> r <sup>c</sup>	127	4700–6900	5087.6	1.00095	0.12909	...
58	15422.276	S <sub>1</sub>	15485.454	Fe <sub>1</sub>	Quadratic Fit	a+br+cr <sup>2</sup>	143	4800–6300	4534.9	243.68	-6.8790	...
59	15422.276	S <sub>1</sub>	15514.279	Fe <sub>1</sub>	Shifted Power Fit	a(r-b) <sup>c</sup>	114	4900–6200	4555.3	-0.86381	0.14224	...
60	15422.276	S <sub>1</sub>	15674.653	Si <sub>1</sub>	Linear Fit	a+br	170	5000–6900	4801.6	147.88	...	...
61	15459.343	Y <sub>1</sub> +V <sub>1?</sub>	15469.816	S <sub>1</sub>	Hoerl Model	a(b') <sup>(r^c)</sup>	157	5000–6600	4699.9	1.0884	-0.22551	...
62	15459.343	Y <sub>1</sub> +V <sub>1?</sub>	15478.482	S <sub>1</sub> +Fe <sub>1</sub>	Hoerl Model	a(b') <sup>(r^c)</sup>	137	4900–6500	4695.0	1.0074	-0.20295	...
63	15462.287	C <sub>01?</sub>	15519.361	Fe <sub>1</sub>	Linear Fit	a+br	74	4900–5700	5748.9	-824.48	...	...
64	15469.816	S <sub>1</sub>	15485.454	Fe <sub>1</sub>	Power Fit	a <sup>b</sup>	81	4900–5600	4787.8	0.11016	...	...
65	15469.816	S <sub>1</sub>	15490.882	Fe <sub>1?</sub>	Shifted Power Fit	a(r-b) <sup>c</sup>	128	4700–6900	2834.5	-3.8666	0.37210	...
66	15469.816	S <sub>1</sub>	15514.279	Fe <sub>1</sub>	Hoerl Model	a(b') <sup>(r^c)</sup>	95	4900–6200	5067.7	1.0068	0.083165	...
67	15469.816	S <sub>1</sub>	15611.045	V <sub>1</sub>	Quadratic Fit	a+br+cr <sup>2</sup>	125	4800–6500	4312.3	771.88	-60.147	...
68	15478.482	S <sub>1</sub>	15490.882	Fe <sub>1?</sub>	Quadratic Fit	a+br+cr <sup>2</sup>	121	4700–6900	4581.2	379.54	-15.872	...
69	15490.882	Fe <sub>1</sub>	15604.221	Fe <sub>1</sub>	Quadratic Fit	a+br+cr <sup>2</sup>	100	4900–5800	6858.0	-4248.8	2260.6	...
70	15490.882	Fe <sub>1</sub>	15621.654	Fe <sub>1</sub>	Quadratic Fit	a+br+cr <sup>2</sup>	107	4900–5750	6878.4	-5478.4	3604.0	...
71	15514.279	Fe <sub>1</sub>	15591.490	Fe <sub>1</sub>	Hoerl Model	a(b') <sup>(r^c)</sup>	98	4900–6150	4394.5	1.0669	-0.16310	...
72	15514.279	Fe <sub>1</sub>	15604.221	Fe <sub>1</sub>	Hoerl Model	a(b') <sup>(r^c)</sup>	116	5000–6100	4371.5	1.1056	-0.19259	...
73	15514.279	Fe <sub>1</sub>	15748.988	Mg <sub>1</sub>	Hoerl Model	a(b') <sup>(r^c)</sup>	135	5000–6300	3963.4	1.2149	-0.17771	...
74	15519.096	Fe <sub>1</sub>	15665.241	Fe <sub>1</sub>	Logarithm Fit	a+bln(r)	117	4900–5750	5702.7	1195.2	...	...
75	15652.871	Fe <sub>1</sub>	15680.069	Cr <sub>1</sub>	Logarithm Fit	a+bln(r)	162	5000–6300	4914.1	1020.1	...	...
76	15658.545	Ti <sub>1</sub>	15661.898	Ti <sub>1</sub> +Fe <sub>1</sub>	Linear Fit	a+br	103	4950–5500	5791.4	-2352.5	...	...
77	15658.545	Ti <sub>1</sub>	15906.044	Fe <sub>1</sub>	Linear Fit	a+br	104	4950–5500	5727.0	-1825.1	...	...
78	15658.545	Ti <sub>1</sub>	15912.591	Fe <sub>1</sub>	Linear Fit	a+br	108	4950–5500	5807.8	-1596.5	...	...
79	15658.545	Ti <sub>1</sub>	15920.637	Fe <sub>1</sub>	Linear Fit	a+br	92	4950–5500	5765.5	-2154.6	...	...
80	15665.240	Fe <sub>1</sub>	15677.519	Fe <sub>1</sub>	Power Fit	a <sup>b</sup>	137	4900–6650	4769.5	-0.24874	...	...
81	15665.240	Fe <sub>1</sub>	15686.441	Fe <sub>1</sub>	Quadratic Fit	a+br+cr <sup>2</sup>	144	4900–6450	7531.9	-5704.6	2994.0	...
82	15665.240	Fe <sub>1</sub>	15748.988	Mg <sub>1</sub>	Shifted Power Fit	a(r-b) <sup>c</sup>	103	5000–6900	4460.3	0.017860	-0.15095	...
83	15673.538	Mn <sub>1+</sub>	15748.988	Mg <sub>1</sub>	Modified Hoerl Model	ab <sup>1/r</sup> r <sup>c</sup>	164	4900–6900	5152.3	1.0760	0.22764	...
84	15748.988	Mg <sub>1</sub>	15941.848	Fe <sub>1</sub>	Modified Hoerl Model	ab <sup>1/r</sup> r <sup>c</sup>	137	4900–6900	6192.5	0.53702	0.056421	...
85	15941.848	Fe <sub>1</sub>	15980.726	Fe <sub>1</sub>	Linear Fit	a+br	179	4700–6900	7359.4	-4381.17	...	...
86	16584.447	V <sub>1</sub>	16632.019	Mg <sub>1</sub> +Fe <sub>1</sub>	Linear Fit	a+br	124	4900–6100	6793.3	-2441.3	...	...
87	16645.874	Fe <sub>1</sub>	16890.414	Fe <sub>1</sub>	Modified Hoerl Model	ab <sup>1/r</sup> r <sup>c</sup>	125	5000–6500	4791.8	0.99914	-0.15115	...

This paper has been typeset from a TeX/LaTeX file prepared by the author.